

# Hidden Zeeman Field in Odd-Parity Magnets: An Ideal Platform for Topological Superconductivity

Xun-Jiang Luo,<sup>1,2,\*</sup> Zi-Ting Sun,<sup>2</sup> Xilin Feng,<sup>2</sup> Mingliang Tian,<sup>1,†</sup> and K. T. Law<sup>2,‡</sup>

<sup>1</sup>High Magnetic Field Laboratory, HFIPS, Chinese Academy of Sciences, Hefei, Anhui 230031, China

<sup>2</sup>Department of Physics, Hong Kong University of Science and Technology, Clear Water Bay, 999077 Hong Kong, China

Odd-parity magnets (OPMs) have emerged as a fundamental class of unconventional magnetisms, characterized by time-reversal-preserving non-relativistic spin splitting (NSS). Despite growing interest, the fundamental understanding of OPMs remains critically incomplete, as previous studies have focused exclusively on NSS while overlooking the intrinsically broken time-reversal symmetry ( $\mathcal{T}$ ) inherent to magnetic order. In this work, we reveal that OPMs universally host a hidden Zeeman field rooted in this  $\mathcal{T}$ -breaking, which fundamentally reshapes their band structure. Through an analytical  $f$ -wave magnet model, we show that NSS microscopically originates from an emergent gauge field, manifesting as a real-space spin loop current order. Crucially, the large NSS (eV scale) enables conventional superconductivity to coexist robustly with the hidden Zeeman field, with Zeeman splitting reaches hundreds of meV. This unique band structure establishes OPMs as an ideal platform for topological superconductors (TSCs), supporting large topological regions. Based on OPMs, we engineer a series of TSCs hosting distinct Majorana boundary modes, including unidirectional Majorana edge states. Our work corrects a fundamental misconception about OPMs and establishes them as a versatile platform for field-free and robust TSCs.

*Introduction.*— Unconventional magnetism, characterized by symmetry-compensated magnetization and substantial non-relativistic spin splitting (NSS), has recently attracted intense interest [1–12]. Among these systems, odd-parity magnets (OPMs) constitute a novel magnetic class which features Rashba-like spin splitting that is odd under momentum inversion [13–23]. Universal spin group symmetry criteria for OPMs have been established, leading to the identification of numerous candidate materials [24, 25]. Experimentally, OPMs have been confirmed in both insulating and metallic compounds [26, 27]. Despite these advances, the fundamental band structure of OPMs remains poorly understood. Previous studies have focused exclusively on the odd-parity NSS, which implicitly preserves time-reversal symmetry  $\mathcal{T}$ . However,  $\mathcal{T}$  is intrinsically broken by the underlying magnetic order. Consequently, a correct description of the band structures of OPMs must simultaneously account for the  $\mathcal{T}$ -preserving NSS and the intrinsic  $\mathcal{T}$ -breaking. Addressing this issue is urgent for this rapidly advancing field and essential to unlock the full potential of OPMs for hosting novel phenomena.

The pursuit of topological superconductors (TSCs) is a central theme in condensed matter physics due to their promising application in topological quantum computation [28–38]. Conventionally, realizing a TSC requires the interplay of three ingredients: superconductivity, spin-orbit coupling (SOC), and broken- $\mathcal{T}$ , typically achieved by an external magnetic field [39–41]. This paradigm has been successfully implemented on various hybrid platforms and great experimental progress has been achieved, notably in superconducting semiconductor systems [42–50]. However, this mainstream strategy faces two major challenges. First, a threshold magnetic field is generally required to drive the topological phase, but strong

fields tend to suppress superconductivity [51]. Second, the achievable Zeeman splitting through the introduced magnetic field is typically limited to the meV scale, resulting in a fragile topological phase that is highly sensitive to disorder [52]. These limitations motivate the search for intrinsic magnetic platforms that are compatible with superconductivity and can support large topological regions in parameter space, a goal that remains crucial and challenging.

In this Letter, we demonstrate that OPMs offer precisely such a platform. This capability stems from their unique band structure, which universally harbors both odd-parity NSS and a hidden Zeeman field (HZF). The HZF arises directly from intrinsic  $\mathcal{T}$ -breaking and manifests as the lifted Kramers degeneracy at time-reversal-invariant momenta [Figs. 1(e) and 1(f)]. Using a representative  $f$ -wave magnet on a triangular lattice [Fig. 1(a)], we reveal the underlying band structure of OPMs by a gauge transformation. In the transformed frame, the magnetic order generates a gauge field, which gives rise to a spin-loop-current order in the real space and the time-reversal-preserving NSS in the momentum space. Meanwhile, a HZF naturally emerges, capturing broken  $\mathcal{T}$ . Crucially, the large NSS (eV scale) pins the spin, enabling conventional superconductivity to robustly coexist with the strong HZF (with Zeeman splitting reaching hundreds of meV). This unique band structure renders OPMs ideal platforms for TSCs, supporting large topological regions. Building on this foundation, we show that introducing  $s$ -wave superconducting pairing to OPMs can engineer various TSCs hosting distinct Majorana boundary modes, such as unidirectional Majorana edge states and spin-group-symmetry-protected Majorana Kramers pairs. Our work provides a correct and complete description of the band structures of OPMs

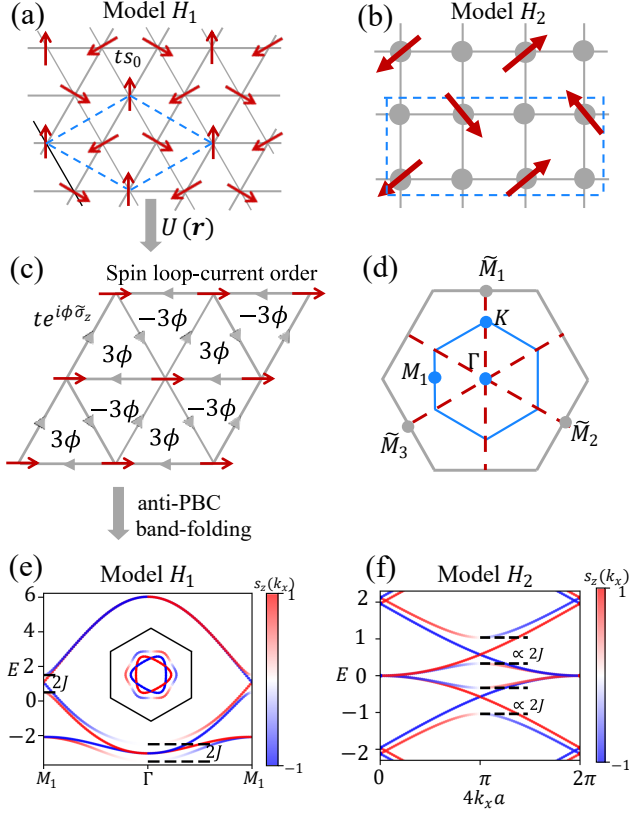


FIG. 1. Band structures of OPMs. (a) and (b) Schematic illustration of models  $H_1$  and  $H_2$ , respectively. The blue dashed lines denote the unit cells. (c) Schematic illustration of mapping  $H_1$  to a spin loop-current order by  $U(\mathbf{r})$ . (d) The plot of Brillouin zones for  $H_1$  (blue) and original triangle lattice (gray). (e) The bulk bands of model  $H_1$  and inset plots its spin textures. (f) The bulk energy bands of model  $H_2$ . In (c),  $\phi = -\pi/3$ . In (c), anti-PBC denotes the abbreviation of anti-periodical boundary conditions. In (e) and (f),  $t = 1$ ,  $J = 0.5$ , and  $\mu = -2.5$  for the inset plot in (e).

and establishes them as an ideal platform for robust and field-free TSCs.

*Band structures of OPMs.*— The NSS in OPMs can be effectively modeled by the term  $\mathbf{S}(\mathbf{k}) \cdot \boldsymbol{\sigma}$ , where  $\mathbf{S}(\mathbf{k}) = -\mathbf{S}(-\mathbf{k})$  and  $\boldsymbol{\sigma} = (\sigma_x, \sigma_y, \sigma_z)$  denote the Pauli matrices in the spin space. However, such a term preserves the time-reversal symmetry  $\mathcal{T}$ , whereas OPMs explicitly break  $\mathcal{T}$ . A direct manifestation of this breaking is the lifting of Kramers degeneracy at time-reversal invariant momenta, as shown in Figs. 1(e) and 1(f). Although certain effective time-reversal operations such as  $\tilde{\mathcal{T}}_1 = \mathcal{T}\tau$  or  $\tilde{\mathcal{T}}_2 = \mathcal{T}\sigma_z$  may be present in OPMs [24], they do not restore the full Kramers degeneracy. Specifically,  $(\tilde{\mathcal{T}}_1)^2 = -e^{ik_x}$  (assuming that  $\tau$  is a half-period translation along  $x$ ) and  $(\tilde{\mathcal{T}}_2)^2 = 1$ ; consequently, only  $\tilde{\mathcal{T}}_1$  can enforce a Kramers degeneracy, and only at  $k_x = 0$  [Fig. 1(f)] [53]. The generic absence of Kramers pairs at time-reversal invariant momenta signals the existence of

a HZF, as we will demonstrate.

To reveal the HZF in OPMs, we first consider a representative model  $H_1$ , as schematically illustrated in Fig. 1(a).  $H_1$  describes an antiferromagnetic order defined on a triangular lattice with a  $\sqrt{3} \times \sqrt{3}$  reconstruction and it takes the form of

$$H_1 = \sum_{\langle \mathbf{r}\mathbf{r}' \rangle, \sigma} t c_{\mathbf{r}\sigma}^\dagger c_{\mathbf{r}'\sigma} + J \sum_{\mathbf{r}, \sigma\sigma'} \mathbf{m}(\mathbf{r}) \cdot \mathbf{c}_{\mathbf{r}\sigma}^\dagger \boldsymbol{\sigma}_{\sigma\sigma'} c_{\mathbf{r}\sigma'}, \quad (1)$$

where  $c_{\mathbf{r}\sigma}^\dagger$  ( $c_{\mathbf{r}\sigma}$ ) creates (annihilates) an electron with spin  $\sigma$  at the position  $\mathbf{r}$ ,  $\langle \mathbf{r}\mathbf{r}' \rangle$  runs over the nearest neighbors with hopping amplitude  $t$ , and the second term describes the exchange coupling to the local moment  $\mathbf{m}(\mathbf{r})$  with strength  $J$ . The magnetic texture is given by  $\mathbf{m}(\mathbf{r}) = (\cos(\mathbf{Q} \cdot \mathbf{r} + \phi), \sin(\mathbf{Q} \cdot \mathbf{r} + \phi), 0)$  with the antiferromagnetic propagation vector  $\mathbf{Q} = \frac{4\pi}{3a}(\frac{1}{2}, \frac{\sqrt{3}}{2})$  and phase offset  $\phi = 7\pi/6$ . Enforced by spin-group symmetries,  $H_1$  realizes an  $f$ -wave magnet with the out plane of spin expectation value of the form  $s_z(\mathbf{k}) \propto k_x(k_x^2 - 3k_y^2)$  while the in-plane spin expectation value  $s_{x,y}(\mathbf{k}) = 0$ , see details in Appendix A.

The HZF in  $H_1$  becomes transparent after a local unitary transformation that rotates all moments to the  $x$ -direction:  $\tilde{H}_1 = UH_1U^\dagger$ , with  $U(\mathbf{r}) = e^{i(\mathbf{Q} \cdot \mathbf{r} + \phi)\sigma_z/2}$ . The transformed Hamiltonian reads

$$\begin{aligned} \tilde{H}_1 = & t \sum_{\mathbf{r}, \sigma} \left[ e^{-i\mathbf{Q} \cdot \mathbf{a}_1 \tilde{\sigma}_z/2} \tilde{c}_\sigma^\dagger(\mathbf{r}) \tilde{c}_\sigma(\mathbf{r} + \mathbf{a}_1) \right. \\ & + e^{-i\mathbf{Q} \cdot \mathbf{a}_2 \tilde{\sigma}_z/2} \tilde{c}_\sigma^\dagger(\mathbf{r}) \tilde{c}_\sigma(\mathbf{r} + \mathbf{a}_2) \\ & \left. + e^{-i\mathbf{Q} \cdot \mathbf{a}_3 \tilde{\sigma}_z/2} \tilde{c}_\sigma^\dagger(\mathbf{r}) \tilde{c}_\sigma(\mathbf{r} + \mathbf{a}_3) + \text{h.c.} \right] \\ & + J \sum_{\mathbf{r}, \sigma\sigma'} \tilde{c}_{\mathbf{r}\sigma}^\dagger (\tilde{\sigma}_x)_{\sigma\sigma'} \tilde{c}_{\mathbf{r}\sigma'}, \end{aligned} \quad (2)$$

where  $\mathbf{a}_1 = (1, 0)a$  (with  $a$  the lattice constant),  $\mathbf{a}_2 = (-1/2, \sqrt{3}/2)a$ ,  $\mathbf{a}_3 = -(\mathbf{a}_2 + \mathbf{a}_1)$ ,  $\tilde{\boldsymbol{\sigma}} = U\boldsymbol{\sigma}U^\dagger$ , and  $\tilde{c}_{\mathbf{r}\sigma} = \sum_{\sigma'} U_{\sigma\sigma'}(\mathbf{r}) c_{\mathbf{r}\sigma'}$ . In  $\tilde{H}_1$ , the exchange coupling term becomes a uniform Zeeman field, which captures the broken  $\mathcal{T}$ . Moreover, an emergent gauge field appears: using  $\mathbf{Q} \cdot \mathbf{a}_1 = \mathbf{Q} \cdot \mathbf{a}_2 = \mathbf{Q} \cdot \mathbf{a}_3 = 2\pi/3 \pmod{2\pi}$ , each hopping term acquires a uniform phase factor  $e^{-i\pi\tilde{\sigma}_z/3}$ . Remarkably, these complex hoppings generate a loop flux on each triangular plaquette [Fig. 1(c)], which corresponds to a spin loop current order in the real space although the charge current on each bond vanishes (see Appendix B for details). Since physical observables are basis-independent, this spin loop current also exists in the original model  $H_1$ .

To gain a deeper understanding, we further analyze the band structures in the momentum space.  $H_1$  has three sublattices and its Bloch Hamiltonian reads

$$H_1 = \begin{pmatrix} -J(\sqrt{3}\sigma_x + \sigma_y)/2 & f(\mathbf{k})\sigma_0 & f^*(\mathbf{k})\sigma_0 \\ f^*(\mathbf{k})\sigma_0 & J(\sqrt{3}\sigma_x - \sigma_y)/2 & f(\mathbf{k})\sigma_0 \\ f(\mathbf{k})\sigma_0 & f^*(\mathbf{k})\sigma_0 & J\sigma_y \end{pmatrix}, \quad (3)$$

where  $f(\mathbf{k}) = t \sum_{i=1}^3 e^{i\mathbf{k}\cdot\mathbf{a}_i}$ . The energy bands of  $H_1(\mathbf{k})$  are plotted in Fig. 1(e); the inset shows the value of  $s_z(\mathbf{k})$ , which exhibits a  $f$ -wave pattern.

We perform two consecutive unitary transformations to block-diagonalize  $H_1(\mathbf{k})$ . The first transformation is

$$U_1 = \text{diag}(e^{i\theta_1\sigma_z}, -e^{i\theta_2\sigma_z}, -e^{i\theta_3\sigma_z}), \quad (4)$$

with  $\theta_1 = 7\pi/12$ ,  $\theta_2 = 11\pi/12$ , and  $\theta_3 = \pi/4$ . Applying  $H'_1(\mathbf{k}) = U_1 H_1(\mathbf{k}) U_1^\dagger$  yields

$$H'_1(\mathbf{k}) = \begin{pmatrix} J\tilde{\sigma}_x & D(\mathbf{k}) & D^\dagger(\mathbf{k}) \\ D^\dagger(\mathbf{k}) & J\tilde{\sigma}_x & D(\mathbf{k}) \\ D(\mathbf{k}) & D^\dagger(\mathbf{k}) & J\tilde{\sigma}_x \end{pmatrix}, \quad (5)$$

where  $D(\mathbf{k}) = -f(\mathbf{k})e^{-i\frac{\pi}{3}\tilde{\sigma}_z}$ . Notably,  $H'_1$  restores translation symmetry due to the cyclic symmetry among sublattices, with the nearest-neighbor hopping becoming  $-te^{-i\pi/3\tilde{\sigma}_z}$ . Thus,  $H'_1(\mathbf{k})$  corresponds to the system described by  $\tilde{H}_1(\mathbf{r})$  with anti-periodic boundary conditions along the  $\mathbf{a}_1$ ,  $\mathbf{a}_2$ , and  $\mathbf{a}_3$  directions, which accounts for the global minus sign in  $D(\mathbf{k})$  [54].

The restored translation symmetry enables further block-diagonalization via a discrete Fourier transform:

$$U_2 = \frac{1}{\sqrt{3}} \begin{pmatrix} \sigma_0 & \sigma_0 & \sigma_0 \\ \sigma_0 & \omega\sigma_0 & \omega^2\sigma_0 \\ \sigma_0 & \omega^2\sigma_0 & \omega\sigma_0 \end{pmatrix}, \quad (6)$$

where  $\omega = e^{2\pi i/3}$ . Transformation  $H''_1 = U_2 H'_1 U_2^\dagger$  gives a block-diagonal Hamiltonian [54]

$$\begin{aligned} H''_1(\mathbf{k}) &= \text{diag}(h_0(\mathbf{k}), h_1(\mathbf{k}), h_2(\mathbf{k})), \\ h_m(\mathbf{k}) &= J\tilde{\sigma}_x + \omega^{-p}D(\mathbf{k}) + \omega^p D^\dagger(\mathbf{k}), \end{aligned} \quad (7)$$

where  $p = 0, 1, 2$  is the sublattice index. These blocks are connected by the magnetic propagation vector  $\mathbf{Q}$ : using  $f(\mathbf{k} + \mathbf{Q}) = \omega f(\mathbf{k})$ , we obtain

$$h_2(\mathbf{k}) = h_0(\mathbf{k} + \mathbf{Q}), \quad h_1(\mathbf{k}) = h_0(\mathbf{k} - \mathbf{Q}). \quad (8)$$

Hence,  $H_1(\mathbf{k})$  exactly maps to a two-band model  $h_0(\mathbf{k})$ ; the energy bands of  $H_1(\mathbf{k})$  are obtained by folding the bands of  $h_0(\mathbf{k})$  into the magnetic Brillouin zone [Fig. 1(d)].  $h_0(\mathbf{k})$  takes the form

$$h_0(\mathbf{k}) = J\tilde{\sigma}_x - f_0(\mathbf{k})\sigma_0 - f_z(\mathbf{k})\tilde{\sigma}_z, \quad (9)$$

where  $f_0(\mathbf{k}) = t \cos k_x a + 2t \cos(k_x a/2) \cos(\sqrt{3}k_y a/2)$  and  $f_z(\mathbf{k}) = \sqrt{3}t (\sin k_x a - 2 \sin(k_x a/2) \cos(\sqrt{3}k_y a/2))$ . The two band model  $h_0(\mathbf{k})$  allows one to obtain the analytical expression for the spin expectation value  $s_{x,y,z}(\mathbf{k})$ . In Appendix C, we show that  $s_{x,y}(\mathbf{k}) = 0$  and  $s_z(\mathbf{k}) = f_z(\mathbf{k})/\sqrt{J^2 + f_z(\mathbf{k})^2}$  (a certain band is considered). Near the  $\Gamma$  point ( $\mathbf{k} = 0$ ),  $s_z(\mathbf{k}) \propto k_x(k_x^2 - 3k_y^2)$ , consistent with the symmetry analysis.

By analytical study of the model  $H_1$ , we uncover several key features that are universal to OPMS. First, the

odd-parity NSS microscopically originates from an emergent gauge field induced by the magnetic order. Second, the energy scales of the NSS and the HZF are set by the hopping amplitude  $t$  and the exchange coupling  $J$ , respectively, which in magnetic materials can reach the eV and hundreds of meV scales. Third, the HZF manifests identically in both the original lattice frame and the rotated frame: it lifts Kramers degeneracy at time-reversal invariant momenta, accounting for the explicit  $\mathcal{T}$ -breaking. Specifically, in the rotated frame, the effective two-band model  $h_0(\mathbf{k})$  exhibits a magnetic gap of  $2J$  opened by the HZF at time-reversal invariant momenta. When folded back into the original magnetic Brillouin zone, this two-band gives rise to six bands. Consequently, only a subset of these bands possess the HZF-induced gap at time-reversal invariant momenta [Fig. 1(e)]; other apparent degeneracies at these momenta are mere artifacts of band folding. Previous works focused on such nodal features but overlooked the band folding effect and the essential role of the HZF [14, 27].

We note that the analytical study of  $H_1$  builds upon the helical magnetic order along the lattice bonds in real space. Such magnetic order is typically realized in helimagnets, which serve as minimal models for  $p$ -wave magnets [15]. These systems can be studied analogously: via a local unitary transformation, they can be mapped onto a two-band model in which both the NSS and HZF are explicitly revealed [54, 55]. However, this mapping is not universally applicable to all OPMS. A notable exception is model  $H_2$ , illustrated in Fig. 1(b), which realizes a  $p$ -wave magnet enforced by certain spin-group symmetries [see the Supplemental Materials (SMs) for details of the Hamiltonian and symmetry analysis]. Figure 1(f) plots the energy bands of  $H_2$ . Direct inspection reveals the lifting of Kramers degeneracy at  $k_x = \pi$  for certain bands, opening a magnetic energy gap proportional to  $2J$ . However, the degeneracy at  $k_x = 0$  remains, protected by the preserved symmetry  $\tilde{\mathcal{T}}_2$  in  $H_2$ . The magnetic energy gap at  $k_x = \pi$  signals the existence of a HZF, which is further supported by the schematic decomposition shown in Fig. 3(c):  $H_2$  can be viewed as a stacking of one-dimensional (1D) helimagnets supplemented by local compensated Zeeman fields. This perspective reinforces that the coexistence of an odd-parity NSS and HZF is a generic hallmark of OPMS.

*Compatibility between OPMS and superconductivity.*—

We now investigate the compatibility of OPMS with superconductivity by performing self-consistent mean-field calculations for models  $H_{1,2}$  with  $s$ -wave pairing. In these systems, the generated gauge field pins the spin along the  $z$ -direction, while the HZF lies in the  $xy$ -plane [56]. This orthogonal configuration is reminiscent of Ising superconductors, where Ising SOC protects superconductivity against large in-plane magnetic fields [57, 58]. We therefore expect superconductivity to persist even for substantial  $J$  in OPMS.

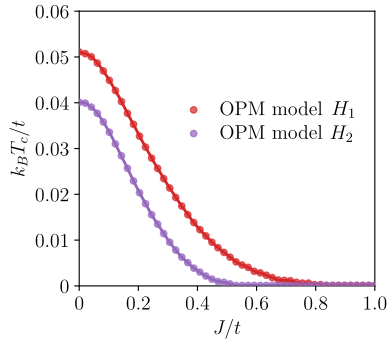


FIG. 2. Self-consistently calculated transition temperature  $T_c$  versus  $J/t$  for model  $H_{\text{BdG}}^{(1,2)}$ . The common model parameters are  $t = 1$ ,  $J = 0.5$ ,  $U = 1.5$ , and  $\mu = -1$ .

To model the superconducting state, we introduce an attractive on-site interaction  $-U$  (with  $U > 0$ ) that mediates a  $s$ -wave pairing. The total Hamiltonian is given by  $H_{\text{SC}}^{(i)} = H_i - U \sum_{\mathbf{r}} c_{\mathbf{r}\uparrow}^\dagger c_{\mathbf{r}\downarrow}^\dagger c_{\mathbf{r}\downarrow} c_{\mathbf{r}\uparrow}$  for  $i = 1, 2$ . Within mean-field theory, we define the order parameter  $\Delta = U \langle c_{\mathbf{r}\downarrow} c_{\mathbf{r}\uparrow} \rangle$ , which leads to the Bogoliubov-de Gennes (BdG) Hamiltonian

$$H_{\text{BdG}}^{(i)}(\mathbf{k}) = \begin{pmatrix} H_i(\mathbf{k}) - \mu & i\Delta\sigma_y \\ -i\Delta^* \sigma_y & -H_i^*(-\mathbf{k}) + \mu \end{pmatrix}, \quad (10)$$

where  $\mu$  is the chemical potential. The critical temperature  $T_c$  is obtained by numerically solving the linearized gap equation  $\partial^2 \mathcal{F}_s(T, \Delta) / \partial \Delta^2 |_{\Delta=0} = 0$ , where  $\mathcal{F}_s$  is the mean-field free energy density.

Figure. 2 shows the normalized critical temperature  $T_c$  for models  $H_{\text{BdG}}^{(1)}$  and  $H_{\text{BdG}}^{(2)}$  as a function of  $J/t$ . In both cases, superconductivity coexists with coplanar magnetic order over a wide range of  $J$ , and  $T_c$  decreases continuously to zero, characteristic of a second-order transition. The robustness of superconductivity in these OPMs stems from the large time-reversal-preserving NSS, which is enforced by certain spin group symmetries.

*Engineering TSCs based on OPMs.*— Diagonalizing  $H_{\text{BdG}}^{(1,2)}$  in a nanowire geometry along the  $y$  direction yields the energy spectra shown in Fig. 3(a) and 3(d), respectively. Both exhibit Majorana flat bands coexisting with gapless bulk states. These flat bands can be understood as follows: at fixed  $k_y = 0$ , the energy bands exhibit a magnetic energy gap at time-reversal invariant momenta. When the chemical potential lies within this gap and a  $s$ -wave pairing is introduced, the corresponding 1D slice enters a TSC phase. As  $k_y$  varies, the model parameters are renormalized and the topological condition is satisfied only within specific  $k_y$  intervals, resulting in a topological nodal superconductor. Using the two-band Hamiltonian  $h_0(\mathbf{k})$ , one can show that the energy spectrum of  $\tilde{H}_{\text{BdG}}^{(2)}$  closes when  $f_z(\mathbf{k}) = 0$  and  $J^2 = \Delta^2 + (f_0 - \mu)^2$  [54]. These conditions are met at points along the  $\Gamma$ - $\tilde{M}_{1,2,3}$  lines where  $f_z(\mathbf{k})$  vanishes, producing six pairs of nodal

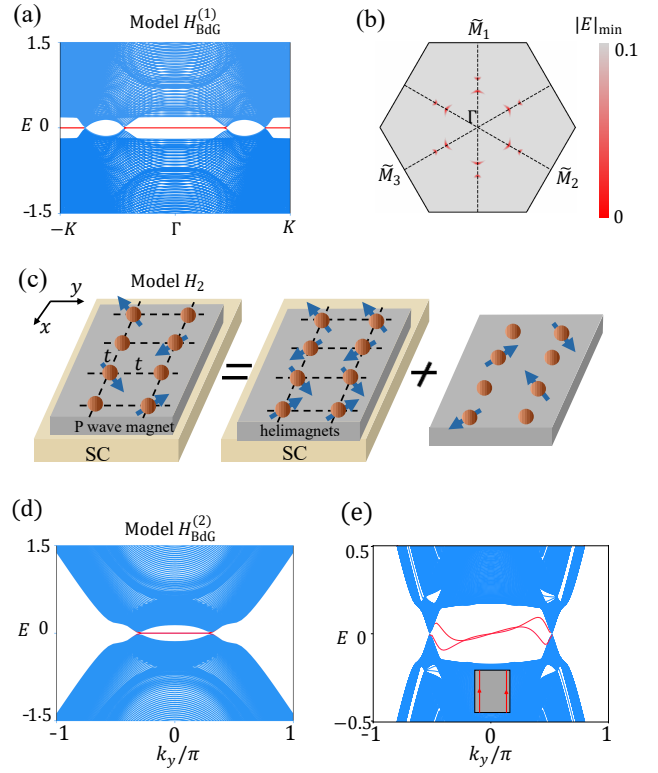


FIG. 3. (a) Energy spectrum of model  $H_{\text{BdG}}^{(2)}$  in a nanowire geometry along the  $y$  direction. (b) Color map of the minimum absolute energy  $|E|_{\text{min}}$  of  $h_0(\mathbf{k})$  with  $s$ -wave pairing. (c) Schematic illustration of model  $H_{\text{BdG}}^{(2)}$ , mapping it to stacked superconducting 1D helimagnets with compensated Zeeman fields. Energy bands of  $H_{\text{BdG}}^{(2)}$  in a nanowire geometry along the  $y$  direction without and with relativistic SOC for (d) and (e), respectively. The model parameters are taken as  $t = 1$ ,  $J = 0.5$ ,  $\Delta = 0.2$ .  $\mu = 1$  for (a) and (b),  $\mu = 3.5$  for (d) and (e).

points in the Brillouin zone, as shown in Fig. 3(b).

The Majorana flat bands in  $H_{\text{BdG}}^{(2)}$  admit another interpretation. As sketched in Fig. 3(c), the model  $H_{\text{BdG}}^{(2)}$  can be decomposed into a stack of superconducting helimagnets with additional compensated Zeeman fields. A stack of superconducting helimagnets hosts nodal points and Majorana flat bands; the extra Zeeman fields merely shift the positions of the bulk nodes while preserving the flat bands [54]. Interestingly, when a relativistic SOC along the  $y$  direction is included, the Majorana flat bands become dispersive edge states, although the bulk nodal points remain [54]. The coexistence of gapless bulk states and dispersive edge states lifts constraints on the propagation direction of edge states, allowing scattering into the bulk. Consequently, edge states on opposite boundaries can propagate either in the same or opposite directions. When they flow in the same direction, unidirectional edge states emerge [59], as illustrated in the inset of Fig. 3(e).

*Discussion and conclusion.*— While we have focused on models  $H_{1,2}$  as concrete examples to reveal the band structures of OPMs and demonstrate the engineering of robust TSCs, the underlying physics is general. This generality stems from the fundamental interplay between spin-group symmetry and time-reversal symmetry breaking in OPMs. In the SMS [54], we further show that OPMs with coplanar or non-coplanar spin textures, distinct from the collinear cases of  $H_{1,2}$ , can similarly realize robust TSCs, provided certain spin-group symmetry conditions are satisfied. Moreover, based on 1D helimagnets realizable in iron atom chains on a superconductor [60], we demonstrate that both Majorana corner states and spin-group-protected Majorana Kramers pairs can be engineered, see details in the SMS [54]. These results establish OPMs as a versatile platform for exploring TSCs.

The use of OPMs as a platform for TSCs offers decisive advantages over conventional approaches relying on external magnetic fields. In standard semiconductor nanowire schemes, the topological phase requires  $m > \sqrt{\Delta^2 + \mu^2}$ , where the Zeeman gap  $m$  is limited to the meV scale (e.g.,  $\sim 1.2$  meV at 10 T for a typical  $g$ -factor of 2). The small Zeeman splitting makes the system extremely sensitive to nonuniform chemical potentials [52]. In stark contrast, OPMs intrinsically host both odd-parity NSS and a HZF. The latter can reach hundreds of meV in real materials, for instance,  $\sim 130$  meV in the  $p$ -wave magnet  $\text{EuIn}_2\text{As}_2$  [54, 61], far exceeding the scale achievable with laboratory fields. This large intrinsic magnetic gap can coexist robustly with superconductivity due to the eV-scale NSS, dramatically expanding the topological regime in parameter space and significantly enhancing the robustness of Majorana boundary modes against disorder.

In summary, we have uncovered a HZF universally present in OPMs, arising directly from their intrinsic time-reversal breaking. This discovery, together with the coexisting large odd-parity NSS, establishes OPMs as an ideal platform for realizing robust and field-free TSCs. Our work resolves a fundamental misconception in the description of OPMs and opens new avenues for exploring Majorana physics in magnetic materials.

#### ACKNOWLEDGMENT

Xun-Jiang Luo thanks for the helpful discussion with Ning Hao. K. T. L. acknowledges the support of the Ministry of Science and Technology, China, The New Cornerstone Foundation, and the Hong Kong Research Grants Council through Grants No. MOST23SC01-A, No. RFS2021-6S03, No. C6053-23G, No. AoE/P-701/20, AoE/P-604/25R, No. 16309223, No. 16311424 and No. 16300325.

- 
- \* [xjluo@hmfl.ac.cn](mailto:xjluo@hmfl.ac.cn)  
 † [tianml@hmfl.ac.cn](mailto:tianml@hmfl.ac.cn)  
 ‡ [phlaw@ust.hk](mailto:phlaw@ust.hk)
- [1] L.-D. Yuan, Z. Wang, J.-W. Luo, E. I. Rashba, and A. Zunger, Giant momentum-dependent spin splitting in centrosymmetric low- $z$  antiferromagnets, *Phys. Rev. B* **102**, 014422 (2020).
  - [2] H.-Y. Ma, M. Hu, N. Li, J. Liu, W. Yao, J.-F. Jia, and J. Liu, Multifunctional antiferromagnetic materials with giant piezomagnetism and noncollinear spin current, *Nature Communications* **12**, 2846 (2021).
  - [3] L. Smejkal, J. Sinova, and T. Jungwirth, Emerging research landscape of altermagnetism, *Phys. Rev. X* **12**, 040501 (2022).
  - [4] P. Liu, J. Li, J. Han, X. Wan, and Q. Liu, Spin-group symmetry in magnetic materials with negligible spin-orbit coupling, *Phys. Rev. X* **12**, 021016 (2022).
  - [5] S.-B. Zhang, L.-H. Hu, and T. Neupert, Finite-momentum cooper pairing in proximitized altermagnets, *Nature Communications* **15**, 1801 (2024).
  - [6] X. Chen, J. Ren, Y. Zhu, Y. Yu, A. Zhang, P. Liu, J. Li, Y. Liu, C. Li, and Q. Liu, Enumeration and representation theory of spin space groups, *Phys. Rev. X* **14**, 031038 (2024).
  - [7] Y. Jiang, Z. Song, T. Zhu, Z. Fang, H. Weng, Z.-X. Liu, J. Yang, and C. Fang, Enumeration of spin-space groups: Toward a complete description of symmetries of magnetic orders, *Phys. Rev. X* **14**, 031039 (2024).
  - [8] Z. Xiao, J. Zhao, Y. Li, R. Shindou, and Z.-D. Song, Spin space groups: Full classification and applications, *Phys. Rev. X* **14**, 031037 (2024).
  - [9] X. Chen, Y. Liu, P. Liu, Y. Yu, J. Ren, J. Li, A. Zhang, and Q. Liu, Unconventional magnons in collinear magnets dictated by spin space groups, *Nature* **640**, 349 (2025).
  - [10] Q. Liu, X. Dai, and S. Blügel, Different facets of unconventional magnetism, *Nature Physics* **21**, 329 (2025).
  - [11] M. Hu, X. Cheng, Z. Huang, and J. Liu, Catalog of  $c$ -paired spin-momentum locking in antiferromagnetic systems, *Phys. Rev. X* **15**, 021083 (2025).
  - [12] X. Feng and Z. Zhang, Superconducting order parameters in spin space groups: Methodology and application, *Phys. Rev. B* **111**, 054520 (2025).
  - [13] S. Hayami, Y. Yanagi, and H. Kusunose, Spontaneous antisymmetric spin splitting in noncollinear antiferromagnets without spin-orbit coupling, *Phys. Rev. B* **101**, 220403 (2020).
  - [14] A. Birk Hellenes, T. Jungwirth, R. Jaeschke-Ubiergo, A. Chakraborty, J. Sinova, and L. Smejkal,  $p$ -wave magnets, [arXiv:2309.01607](https://arxiv.org/abs/2309.01607).
  - [15] B. Brekke, P. Sukhachov, H. G. Giil, A. Brataas, and J. Linder, Minimal models and transport properties of unconventional  $p$ -wave magnets, *Phys. Rev. Lett.* **133**, 236703 (2024).
  - [16] Y. Yu, M. B. Lyngby, T. Shishidou, M. Roig, A. Kreisler, M. Weinert, B. M. Andersen, and D. F. Agterberg, Odd-parity magnetism driven by antiferromagnetic exchange, *Phys. Rev. Lett.* **135**, 046701 (2025).
  - [17] C. Lee and P. M. R. Brydon, Inversion-asymmetric itinerant antiferromagnets by the space group symmetry, *Phys. Rev. Lett.* **135**, 116701 (2025).

- [18] Y.-P. Lin, Odd-parity altermagnetism through sublattice currents: From Haldane-Hubbard model to general bipartite lattices, [arXiv:2503.09602 \(2025\)](#).
- [19] S. Huang, Z. Qin, F. Zhan, D.-H. Xu, D.-S. Ma, and R. Wang, Light-induced Odd-parity Magnetism in Conventional Collinear Antiferromagnets, [arXiv:2507.20705 \(2025\)](#).
- [20] B. Li, D.-F. Shao, and A. A. Kovalev, Floquet Spin Splitting and Spin Generation in Antiferromagnets, [arXiv:2507.22884 \(2025\)](#).
- [21] T. Zhu, D. Zhou, H. Wang, and J. Ruan, Floquet odd-parity collinear magnets, [arXiv:2508.02542 \(2025\)](#).
- [22] Z.-Y. Zhuang, D. Zhu, D. Liu, Z. Wu, and Z. Yan, Odd-Parity Altermagnetism Originated from Orbital Orders, [arXiv:2508.18361 \(2025\)](#).
- [23] D. Liu, Z.-Y. Zhuang, D. Zhu, Z. Wu, and Z. Yan, Light-induced odd-parity altermagnets on dimerized lattices, [arXiv:2508.18360 \(2025\)](#).
- [24] X.-J. Luo, J.-X. Hu, and K. T. Law, Spin Symmetry Criteria for Odd-parity Magnets, [arXiv:2510.05512 \(2025\)](#).
- [25] Z. Song, Z. Qi, C. Fang, Z. Fang, and H. Weng, A Unified Symmetry Classification of Magnetic Orders via Spin Space Groups: Prediction of Coplanar Even-Wave Phases, [arXiv:2512.08901 \(2025\)](#).
- [26] Q. Song, S. Stavrić, P. Barone, A. Droghetti, D. S. Antonenko, J. W. F. Venderbos, C. A. Occhialini, B. Ilyas, E. Ergeçen, N. Gedik, S.-W. Cheong, R. M. Fernandes, S. Picozzi, and R. Comin, Electrical switching of a p-wave magnet, *Nature* **642**, 64 (2025).
- [27] R. Yamada, M. T. Birch, P. R. Baral, S. Okumura, R. Nakano, S. Gao, M. Ezawa, T. Nomoto, J. Masell, Y. Ishihara, K. K. Kolincio, I. Belopolski, H. Sagayama, H. Nakao, K. Ohishi, T. Ohhara, R. Kiyonagi, T. Nakajima, Y. Tokura, T.-h. Arima, Y. Motome, M. M. Hirschmann, and M. Hirschberger, A metallic p-wave magnet with commensurate spin helix, *Nature* **646**, 837 (2025).
- [28] A. Y. Kitaev, Unpaired majorana fermions in quantum wires, *Physics-Uspekhi* **44**, 131 (2001).
- [29] L. Fu and C. L. Kane, Superconducting proximity effect and majorana fermions at the surface of a topological insulator, *Phys. Rev. Lett.* **100**, 096407 (2008).
- [30] X.-L. Qi, T. L. Hughes, and S.-C. Zhang, Topological field theory of time-reversal invariant insulators, *Phys. Rev. B* **78**, 195424 (2008).
- [31] C. Nayak, S. H. Simon, A. Stern, M. Freedman, and S. Das Sarma, Non-abelian anyons and topological quantum computation, *Rev. Mod. Phys.* **80**, 1083 (2008).
- [32] M. Z. Hasan and C. L. Kane, Colloquium: Topological insulators, *Reviews of Modern Physics* **82**, 3045 (2010).
- [33] X.-J. Luo, X.-H. Pan, and X. Liu, Higher-order topological superconductors based on weak topological insulators, *Phys. Rev. B* **104**, 104510 (2021).
- [34] X.-J. Luo, W.-X. Qiu, and F. Wu, Majorana zero modes in twisted transition metal dichalcogenide homobilayers, *Phys. Rev. B* **109**, L041103 (2024).
- [35] X.-H. Pan, L. Chen, D. E. Liu, F.-C. Zhang, and X. Liu, Majorana zero modes induced by the meissner effect at small magnetic field, *Phys. Rev. Lett.* **132**, 036602 (2024).
- [36] Z. Zhang, Z. Wu, C. Fang, F.-c. Zhang, J. Hu, Y. Wang, and S. Qin, Topological superconductivity from unconventional band degeneracy with conventional pairing, *Nature Communications* **15**, 7971 (2024).
- [37] X.-J. Luo, X.-H. Pan, Y. Shi, and F. Wu, Surface-dependent majorana vortex phases in topological crystalline insulators, *Phys. Rev. B* **111**, 144501 (2025).
- [38] X.-J. Luo, Majorana vortex phases in time-reversal invariant higher-order topological insulators and topologically trivial insulators, [arXiv:2505.17980 \(2025\)](#).
- [39] J. Alicea, New directions in the pursuit of majorana fermions in solid state systems, *Reports on Progress in Physics* **75**, 076501 (2012).
- [40] S. R. Elliott and M. Franz, Colloquium: Majorana fermions in nuclear, particle, and solid-state physics, *Rev. Mod. Phys.* **87**, 137 (2015).
- [41] X.-H. Pan, K.-J. Yang, L. Chen, G. Xu, C.-X. Liu, and X. Liu, Lattice-symmetry-assisted second-order topological superconductors and majorana patterns, *Phys. Rev. Lett.* **123**, 156801 (2019).
- [42] J. D. Sau, R. M. Lutchyn, S. Tewari, and S. Das Sarma, Generic new platform for topological quantum computation using semiconductor heterostructures, *Phys. Rev. Lett.* **104**, 040502 (2010).
- [43] Y. Oreg, G. Refael, and F. von Oppen, Helical liquids and majorana bound states in quantum wires, *Phys. Rev. Lett.* **105**, 177002 (2010).
- [44] R. M. Lutchyn, J. D. Sau, and S. Das Sarma, Majorana fermions and a topological phase transition in semiconductor-superconductor heterostructures, *Phys. Rev. Lett.* **105**, 077001 (2010).
- [45] A. Das, Y. Ronen, Y. Most, Y. Oreg, M. Heiblum, and H. Shtrikman, Zero-bias peaks and splitting in an alinas nanowire topological superconductor as a signature of majorana fermions, *Nature Physics* **8**, 887 (2012).
- [46] X. Liu, X. Li, D.-L. Deng, X.-J. Liu, and S. Das Sarma, Majorana spintronics, *Phys. Rev. B* **94**, 014511 (2016).
- [47] M. Hell, M. Leijnse, and K. Flensberg, Two-dimensional platform for networks of majorana bound states, *Phys. Rev. Lett.* **118**, 107701 (2017).
- [48] F. Pientka, A. Keselman, E. Berg, A. Yacoby, A. Stern, and B. I. Halperin, Topological superconductivity in a planar josephson junction, *Phys. Rev. X* **7**, 021032 (2017).
- [49] R. M. Lutchyn, E. P. A. M. Bakkers, L. P. Kouwenhoven, P. Krogstrup, C. M. Marcus, and Y. Oreg, Majorana zero modes in superconductor-semiconductor heterostructures, *Nature Reviews Materials* **3**, 52 (2018).
- [50] A. Fornieri, A. M. Whiticar, F. Setiawan, E. Portolés, A. C. C. Drachmann, A. Keselman, S. Gronin, C. Thomas, T. Wang, R. Kallaher, G. C. Gardner, E. Berg, M. J. Manfra, A. Stern, C. M. Marcus, and F. Nichele, Evidence of topological superconductivity in planar josephson junctions, *Nature* **569**, 89 (2019).
- [51] Z. Zhu, M. Papa, X.-A. Nie, H.-K. Xu, Y.-S. Gu, X. Yang, D. Guan, S. Wang, Y. Li, C. Liu, J. Luo, Z.-A. Xu, H. Zheng, L. Fu, and J.-F. Jia, Discovery of segmented fermi surface induced by cooper pair momentum, *Science* **374**, 1381 (2021).
- [52] C.-X. Liu, J. D. Sau, T. D. Stanescu, and S. Das Sarma, Andreev bound states versus majorana bound states in quantum dot-nanowire-superconductor hybrid structures: Trivial versus topological zero-bias conductance peaks, *Phys. Rev. B* **96**, 075161 (2017).
- [53] Y. B. Kudasov, Topological band structure due to modified kramers degeneracy for electrons in a helical magnetic field, *Phys. Rev. B* **109**, L140402 (2024).

- [54] See the Supplemental Materials for the details of the band structures of model  $H_1$ ; details of model  $H_2$ ; topological superconductors based on models  $H_{1,2}$ ; engineering TSCs based on 1D Odd-parity magnets; engineer Majorana corner states and Kramers pair; band structure of the  $p$ -wave magnet  $\text{EuIn}_2\text{As}_2$ .
- [55] I. Martin and A. F. Morpurgo, Majorana fermions in superconducting helical magnets, *Phys. Rev. B* **85**, 144505 (2012).
- [56] Z.-T. Sun, X. Feng, Y.-M. Xie, B. T. Zhou, J.-X. Hu, and K. T. Law, Pseudo-ising superconductivity induced by  $p$ -wave magnetism, *Phys. Rev. B* **112**, 214504 (2025).
- [57] J. M. Lu, O. Zheliuk, I. Leermakers, N. F. Q. Yuan, U. Zeitler, K. T. Law, and J. T. Ye, Evidence for two-dimensional ising superconductivity in gated  $\text{mos}_2/\text{Bi}_2\text{Se}_3/\text{Bi}_2\text{Se}_3$ , *Science* **350**, 1353 (2015).
- [58] X. Xi, Z. Wang, W. Zhao, J.-H. Park, K. T. Law, H. Berger, L. Forró, J. Shan, and K. F. Mak, Ising pairing in superconducting  $\text{NbSe}_2$  atomic layers, *Nature Physics* **12**, 139 (2016).
- [59] C. L. M. Wong, J. Liu, K. T. Law, and P. A. Lee, Majorana flat bands and unidirectional majorana edge states in gapless topological superconductors, *Phys. Rev. B* **88**, 060504 (2013).
- [60] S. Nadj-Perge, I. K. Drozdov, B. A. Bernevig, and A. Yazdani, Proposal for realizing majorana fermions in chains of magnetic atoms on a superconductor, *Phys. Rev. B* **88**, 020407 (2013).
- [61] N. A. A. Pari, R. Jaeschke-Ubiergo, A. Chakraborty, L. Smejkal, and J. Sinova, Nonrelativistic linear edelstein effect in helical  $\text{EuIn}_2\text{As}_2$ , *Phys. Rev. B* **112**, 024404 (2025).
- [62] Y. Xie, B. T. Zhou, T. K. Ng, and K. T. Law, Strongly enlarged topological regime and enhanced superconducting gap in nanowires coupled to ising superconductors, *Phys. Rev. Res.* **2**, 013026 (2020).
- [63] Z.-T. Sun, X. Feng, Y.-M. Xie, B. T. Zhou, J.-X. Hu, and K. T. Law, Pseudo-ising superconductivity induced by  $p$ -wave magnetism, *Phys. Rev. B* **112**, 214504 (2025).
- [64] P. Sukhachov, H. G. Gil, B. Brekke, and J. Linder, Coexistence of  $p$ -wave magnetism and superconductivity, *Phys. Rev. B* **111**, L220403 (2025).
- [65] J. Klinovaja, P. Stano, A. Yazdani, and D. Loss, Topological superconductivity and majorana fermions in rkky systems, *Phys. Rev. Lett.* **111**, 186805 (2013).
- [66] D. Yamaguchi, A. Kitaori, N. Nagaosa, and Y. Tokura, Current control of spin helicity and nonreciprocal charge transport in a multiferroic conductor, *Advanced Materials* **37**, 2420614 (2025).
- [67] X.-J. Luo, J.-Z. Li, M. Xiao, and F. Wu, Characterization of higher-order topological superconductors using both indices, *Phys. Rev. B* **111**, 184516 (2025).

## End Matter

*Appendix A: Symmetry constraints on the spin textures.*— In this appendix, we identify  $H_1$  as a  $f$ -wave magnet by symmetry considerations.  $H_1$  respects the effective time-reversal symmetry  $\tilde{T}_2 = \mathcal{T}\sigma_z$ , the spin-group symmetries  $g_1 = \{U_z(2\pi/3)|\tau_1\}$  (where  $\tau_1$  is a one-third-period translation along  $x$ ),  $g_2 = \{I|R_3\}$  (with  $R_3$  denoting a spatial threefold rotation by  $2\pi/3$  about the  $z$  axis), and  $g_3 = \{U_y(\pi)|M_x\}$ , where  $M_x$  is a mirror reflection  $x \rightarrow -x$ . These symmetries impose constraints on the spin expectation values  $s_\alpha(\mathbf{k}) = \langle \psi_{\mathbf{k}} | \sigma_\alpha | \psi_{\mathbf{k}} \rangle$  ( $\alpha = x, y, z$ ) as follows:

$$\begin{aligned} \tilde{T}_2 : s_z(\mathbf{k}) &= -s_z(-\mathbf{k}), & s_{x,y}(\mathbf{k}) &= s_{x,y}(-\mathbf{k}), \\ g_1 : s_{x,y}(\mathbf{k}) &= 0, \\ g_2 : s_z(R_3\mathbf{k}) &= s_z(\mathbf{k}), \\ g_3 : s_z(M_x\mathbf{k}) &= -s_z(\mathbf{k}), \end{aligned} \quad (\text{A1})$$

where  $|\psi_{\mathbf{k}}\rangle$  are the Bloch states at momentum  $\mathbf{k}$ .

To obtain the explicit form of  $s_z(\mathbf{k})$ , we expand it in angular harmonics. Writing  $\mathbf{k} = (k \cos \theta, k \sin \theta)$  with  $k = |\mathbf{k}|$ , we have the general expansion

$$s_z(\mathbf{k}) = \sum_{l=0}^{\infty} [a_l(k) \cos(l\theta) + b_l(k) \sin(l\theta)], \quad (\text{A2})$$

where  $a_l(k)$  and  $b_l(k)$  are radial functions. The symmetry constraints restrict the allowed harmonics. The condition  $s_z(\mathbf{k}) = -s_z(-\mathbf{k})$  requires  $l$  to be odd. The condition  $s_z(R_3\mathbf{k}) = s_z(\mathbf{k})$  demands invariance under  $\theta \rightarrow \theta + 2\pi/3$ , which forces  $l$  to be multiples of 3. Together with odd  $l$ , the allowed harmonics are  $l = 3, 9, 15, \dots$ . Finally, the mirror symmetry  $g_3$  imposes  $s_z(M_x\mathbf{k}) = -s_z(\mathbf{k})$ . Under  $M_x$ ,  $\theta \rightarrow \pi - \theta$ . Using  $\cos(3(\pi - \theta)) = -\cos(3\theta)$  and  $\sin(3(\pi - \theta)) = \sin(3\theta)$ , we find that  $a_3(k)$  can be nonzero while  $b_3(k)$  must vanish. Hence, the leading term at small  $k$  is

$$s_z(\mathbf{k}) = a_3(k) \cos(3\theta) + \mathcal{O}(k^9), \quad (\text{A3})$$

with  $a_3(k) \propto k^3$ . In Cartesian coordinates,  $\cos(3\theta) = (k_x^3 - 3k_x k_y^2)/k^3$ , yielding

$$s_z(\mathbf{k}) \propto k_x(k_x^2 - 3k_y^2) + \mathcal{O}(k^9). \quad (\text{A4})$$

This  $f$ -wave angular dependence identifies  $H_1$  as an  $f$ -wave magnet.

*Appendix B: Spin loop-current order.*— In this appendix, we demonstrate that the transformed Hamiltonian  $\tilde{H}_1$  hosts a spin loop-current order, and that this order is physically equivalent to that in the original model  $H_1$ . The model Hamiltonian  $\tilde{H}_1(\mathbf{r})$  can be written as

$$\begin{aligned} \tilde{H}_1 &= \tilde{H}_{\text{hop}} + J \sum_{\mathbf{r}, \sigma\sigma'} \tilde{c}_{\mathbf{r}\sigma}^\dagger (\tilde{\sigma}_x)_{\sigma\sigma'} \tilde{c}_{\mathbf{r}\sigma'}, \\ \tilde{H}_{\text{hop}} &= t \sum_{\mathbf{r}, \sigma} \sum_{\boldsymbol{\delta}} \tilde{\omega}_{\boldsymbol{\delta}} \tilde{c}_{\mathbf{r}\sigma}^\dagger \tilde{c}_{\mathbf{r}+\boldsymbol{\delta}, \sigma}, \end{aligned} \quad (\text{B1})$$

where the sum over  $\boldsymbol{\delta}$  runs over all six nearest-neighbor vectors of the triangular lattice:  $\boldsymbol{\delta} = \pm\mathbf{a}_1, \pm\mathbf{a}_2, \pm\mathbf{a}_3$ . The phase factor is  $\tilde{\omega}_{\boldsymbol{\delta}} = e^{-i\sigma\pi/3}$  for  $\boldsymbol{\delta} = \mathbf{a}_i$  and  $\tilde{\omega}_{\boldsymbol{\delta}} = e^{i\sigma\pi/3}$  for  $\boldsymbol{\delta} = -\mathbf{a}_i$ , ensuring  $\tilde{\omega}_{-\boldsymbol{\delta}} = \tilde{\omega}_{\boldsymbol{\delta}}^*$ . Here  $\sigma = +1$  ( $\sigma = -1$ ) denotes spin  $\uparrow$  ( $\downarrow$ ).

To derive the current operator, we consider the Heisenberg equation of motion ( $\hbar = 1$ )

$$\frac{d}{dt} \tilde{n}_{\mathbf{r}} = i[\tilde{H}, \tilde{n}_{\mathbf{r}}] = i[\tilde{H}_{\text{hop}}, \tilde{n}_{\mathbf{r}}], \quad (\text{B2})$$

where the particle number operator is  $\tilde{n}_{\mathbf{r}} = \sum_{\tau} \tilde{c}_{\mathbf{r}\tau}^\dagger \tilde{c}_{\mathbf{r}\tau}$ . The on-site Zeeman term commutes with  $\tilde{n}_{\mathbf{r}}$  because it is local and conserves the particle number.

Using the fermionic commutator identity with spin indices,

$$[\tilde{c}_{i\sigma_1}^\dagger \tilde{c}_{j\sigma_2}, \tilde{c}_{k\sigma_3}^\dagger \tilde{c}_{l\sigma_4}] = \delta_{jk} \delta_{\sigma_2\sigma_3} \tilde{c}_{i\sigma_1}^\dagger \tilde{c}_{l\sigma_4} - \delta_{il} \delta_{\sigma_1\sigma_4} \tilde{c}_{k\sigma_3}^\dagger \tilde{c}_{j\sigma_2}, \quad (\text{B3})$$

we evaluate the commutator for each bond. For a fixed site  $\mathbf{r}$  and a fixed nearest-neighbor vector  $\boldsymbol{\delta}$ , the term  $\tilde{\omega}_{\boldsymbol{\delta}} \tilde{c}_{\mathbf{r}\sigma}^\dagger \tilde{c}_{\mathbf{r}+\boldsymbol{\delta}, \sigma}$  gives a contribution  $-\tilde{\omega}_{\boldsymbol{\delta}} \tilde{c}_{\mathbf{r}\sigma}^\dagger \tilde{c}_{\mathbf{r}+\boldsymbol{\delta}, \sigma}$  to  $[\tilde{H}_{\text{hop}}, \tilde{n}_{\mathbf{r}}]$ , while its Hermitian conjugate  $\tilde{\omega}_{\boldsymbol{\delta}}^* \tilde{c}_{\mathbf{r}+\boldsymbol{\delta}, \sigma}^\dagger \tilde{c}_{\mathbf{r}\sigma}$  gives  $+\tilde{\omega}_{\boldsymbol{\delta}}^* \tilde{c}_{\mathbf{r}+\boldsymbol{\delta}, \sigma}^\dagger \tilde{c}_{\mathbf{r}\sigma}$ . Summing over all  $\boldsymbol{\delta}$  and spin  $\sigma$ , we obtain

$$[\tilde{H}_{\text{hop}}, \tilde{n}_{\mathbf{r}}] = t \sum_{\boldsymbol{\delta}, \sigma} \left( -\tilde{\omega}_{\boldsymbol{\delta}} \tilde{c}_{\mathbf{r}\sigma}^\dagger \tilde{c}_{\mathbf{r}+\boldsymbol{\delta}, \sigma} + \tilde{\omega}_{\boldsymbol{\delta}}^* \tilde{c}_{\mathbf{r}+\boldsymbol{\delta}, \sigma}^\dagger \tilde{c}_{\mathbf{r}\sigma} \right). \quad (\text{B4})$$

Hence, the Heisenberg equation becomes

$$\frac{d}{dt} \tilde{n}_{\mathbf{r}} = it \sum_{\boldsymbol{\delta}, \sigma} \left( -\tilde{\omega}_{\boldsymbol{\delta}} \tilde{c}_{\mathbf{r}\sigma}^\dagger \tilde{c}_{\mathbf{r}+\boldsymbol{\delta}, \sigma} + \tilde{\omega}_{\boldsymbol{\delta}}^* \tilde{c}_{\mathbf{r}+\boldsymbol{\delta}, \sigma}^\dagger \tilde{c}_{\mathbf{r}\sigma} \right). \quad (\text{B5})$$

To cast this as a continuity equation  $\frac{d}{dt} \tilde{n}_{\mathbf{r}} = -\sum_{\boldsymbol{\delta}} (\tilde{J}_{\mathbf{r} \rightarrow \mathbf{r}+\boldsymbol{\delta}} - \tilde{J}_{\mathbf{r}+\boldsymbol{\delta} \rightarrow \mathbf{r}})$ , we define the charge current operator from  $\mathbf{r}$  to  $\mathbf{r} + \boldsymbol{\delta}$  as

$$\tilde{J}_{\mathbf{r} \rightarrow \mathbf{r}+\boldsymbol{\delta}} = \frac{it}{2} \left( \tilde{\omega}_{\boldsymbol{\delta}} \tilde{c}_{\mathbf{r}\sigma}^\dagger \tilde{c}_{\mathbf{r}+\boldsymbol{\delta}, \sigma} - \tilde{\omega}_{\boldsymbol{\delta}}^* \tilde{c}_{\mathbf{r}+\boldsymbol{\delta}, \sigma}^\dagger \tilde{c}_{\mathbf{r}\sigma} \right). \quad (\text{B6})$$

This operator is Hermitian and satisfies  $\tilde{J}_{\mathbf{r}+\boldsymbol{\delta} \rightarrow \mathbf{r}} = -\tilde{J}_{\mathbf{r} \rightarrow \mathbf{r}+\boldsymbol{\delta}}$ . Similarly, the spin current operator for the  $z$ -component is defined by:

$$\tilde{J}_{\mathbf{r} \rightarrow \mathbf{r}+\boldsymbol{\delta}}^z = \frac{it}{2} \sum_{\sigma} \sigma \left( \tilde{\omega}_{\boldsymbol{\delta}} \tilde{c}_{\mathbf{r}\sigma}^\dagger \tilde{c}_{\mathbf{r}+\boldsymbol{\delta}, \sigma} - \tilde{\omega}_{\boldsymbol{\delta}}^* \tilde{c}_{\mathbf{r}+\boldsymbol{\delta}, \sigma}^\dagger \tilde{c}_{\mathbf{r}\sigma} \right). \quad (\text{B7})$$

The expectation value of the charge current in the ground state  $|\tilde{\Psi}_0\rangle$  is

$$\langle \tilde{J}_{\mathbf{r} \rightarrow \mathbf{r}+\boldsymbol{\delta}} \rangle = \frac{it}{2} \sum_{\sigma} \left( \tilde{\omega}_{\boldsymbol{\delta}} A_{\sigma}(\boldsymbol{\delta}) - \tilde{\omega}_{\boldsymbol{\delta}}^* A_{\sigma}^*(\boldsymbol{\delta}) \right), \quad (\text{B8})$$

where  $A_{\sigma}(\boldsymbol{\delta}) = \langle \tilde{c}_{\mathbf{r}\sigma}^\dagger \tilde{c}_{\mathbf{r}+\boldsymbol{\delta}, \sigma} \rangle$  (translation invariance makes it independent of  $\mathbf{r}$ ). The Hamiltonian  $\tilde{H}_1$  possesses the

anti-unitary symmetry  $\Theta = i\tilde{\sigma}_x\mathcal{K}$  (with  $\mathcal{K}$  being a complex conjugation), which satisfies  $\Theta\tilde{H}_1\Theta^{-1} = \tilde{H}_1$  and exchanges spin up and down. This symmetry implies

$$A_{-\sigma}(\boldsymbol{\delta}) = A_{\sigma}^*(\boldsymbol{\delta}). \quad (\text{B9})$$

Using this relation, one finds that the two spin contributions in  $\langle\tilde{J}\rangle$  cancel exactly, giving  $\langle\tilde{J}_{\mathbf{r}\rightarrow\mathbf{r}+\boldsymbol{\delta}}\rangle = 0$  for every bond.

For the spin current, the extra factor  $\sigma$  prevents cancellation. Using  $A_{-\sigma} = A_{\sigma}^*$  and summing over  $\sigma$ , we obtain that

$$\langle\tilde{J}_{\mathbf{r}\rightarrow\mathbf{r}+\boldsymbol{\delta}}^z\rangle = it(e^{-i\pi/3}A_+(\boldsymbol{\delta}) - e^{i\pi/3}A_+^*(\boldsymbol{\delta})), \quad (\text{B10})$$

which is generally nonzero and purely real. Consequently, each bond carries a persistent spin current.

We now consider an elementary triangular plaquette formed by sites  $\mathbf{r}_1, \mathbf{r}_2, \mathbf{r}_3$  in counter-clockwise order, with bonds along  $\mathbf{a}_1, \mathbf{a}_2, \mathbf{a}_3$  completing the triangle. The total spin current circulating around this plaquette is

$$\tilde{J}_{\Delta}^z = \tilde{J}_{\mathbf{r}_1\rightarrow\mathbf{r}_2}^z + \tilde{J}_{\mathbf{r}_2\rightarrow\mathbf{r}_3}^z + \tilde{J}_{\mathbf{r}_3\rightarrow\mathbf{r}_1}^z. \quad (\text{B11})$$

Because each bond carries the same magnitude of spin current, the sum is nonzero, indicating a spin loop-current order.

The original Hamiltonian  $H_1$  is related to  $\tilde{H}_1$  by the unitary transformation  $U(\mathbf{r})$ . For any observable  $O$  in the original frame, its expectation value satisfies

$$\langle\Psi_0|O|\Psi_0\rangle = \langle\tilde{\Psi}_0|UOU^\dagger|\tilde{\Psi}_0\rangle,$$

where  $|\Psi_0\rangle = U^\dagger|\tilde{\Psi}_0\rangle$  is the ground state of  $H_1$ . The physical spin current operator in the laboratory frame is  $J_{\mathbf{r}\rightarrow\mathbf{r}+\mathbf{a}_i}^{z,\text{lab}} = U^\dagger\tilde{J}_{\mathbf{r}\rightarrow\mathbf{r}+\mathbf{a}_i}^zU$ . Since  $U$  is a spin rotation about the  $z$ -axis, it commutes with  $\sigma_z$  and therefore leaves the spin current operator unchanged. Consequently,

$$\langle\Psi_0|J_{\mathbf{r}\rightarrow\mathbf{r}+\mathbf{a}_i}^{z,\text{lab}}|\Psi_0\rangle = \langle\tilde{\Psi}_0|\tilde{J}_{\mathbf{r}\rightarrow\mathbf{r}+\mathbf{a}_i}^z|\tilde{\Psi}_0\rangle. \quad (\text{B12})$$

Thus, the spin loop-current order exists in the original model as well, confirming its physical reality.

*Appendix C: Analytical calculations of the spin textures* .— In this appendix, we analytically compute the spin expectation values  $s_{x,y,z}(\mathbf{k})$  for  $H_1(\mathbf{k})$ . Recall that after the sequence of unitary transformations  $U_1$  and  $U_2$ , the Hamiltonian becomes block-diagonal:

$$\begin{aligned} H_1''(\mathbf{k}) &= U_2U_1H_1(\mathbf{k})U_1^\dagger U_2^\dagger \\ &= \text{diag}(h_0(\mathbf{k}), h_1(\mathbf{k}), h_2(\mathbf{k})), \end{aligned} \quad (\text{C1})$$

where each  $h_p(\mathbf{k})$  ( $p = 0, 1, 2$ ) is a  $2 \times 2$  matrix acting on the spin space. Concretely,

$$h_p(\mathbf{k}) = J\tilde{\sigma}_x - f_0^{(p)}(\mathbf{k})\sigma_0 - f_z^{(p)}(\mathbf{k})\tilde{\sigma}_z, \quad (\text{C2})$$

with

$$\begin{aligned} f_0^{(0)}(\mathbf{k}) &= f_0(\mathbf{k}), \quad f_z^{(0)}(\mathbf{k}) = f_z(\mathbf{k}), \\ f_0^{(1)}(\mathbf{k}) &= f_0(\mathbf{k} - \mathbf{Q}), \quad f_z^{(1)}(\mathbf{k}) = f_z(\mathbf{k} - \mathbf{Q}), \\ f_0^{(2)}(\mathbf{k}) &= f_0(\mathbf{k} + \mathbf{Q}), \quad f_z^{(2)}(\mathbf{k}) = f_z(\mathbf{k} + \mathbf{Q}), \end{aligned} \quad (\text{C3})$$

It is noted that the tilde on  $\tilde{\sigma}_x$  and  $\tilde{\sigma}_z$  indicates that these Pauli matrices are expressed in the rotated spin basis.

Let  $|\chi_p^\tau(\mathbf{k})\rangle$  be an eigenstate of  $h_p(\mathbf{k})$  with band index  $\tau = \pm$ . The eigenstate  $|\psi_{\mathbf{k}}\rangle$  can be written as

$$|\psi_{\mathbf{k}}\rangle = U_1^\dagger U_2^\dagger (|\chi_p^\tau\rangle \otimes |p\rangle), \quad (\text{C4})$$

where  $|p\rangle$  denotes the sublattice index in the Fourier basis.

We first consider the out-of-plane component  $s_z(\mathbf{k})$ . Because  $[U_{1,2}, \sigma_z]$ , we have

$$\begin{aligned} s_z(\mathbf{k}) &= \langle\psi_{\mathbf{k}}|\sigma_z|\psi_{\mathbf{k}}\rangle = \langle\chi_m^\tau|\tilde{\sigma}_z|\chi_m^\tau\rangle \\ &= \tau \frac{f_z^{(m)}}{\sqrt{J^2 + (f_z^{(m)})^2}}. \end{aligned} \quad (\text{C5})$$

For the in-plane component  $s_x(\mathbf{k})$ , we have

$$\begin{aligned} s_x(\mathbf{k}) &= \langle\psi_{\mathbf{k}}|\sigma_x|\psi_{\mathbf{k}}\rangle \\ &= \sum_{p'} |(U_2^\dagger)_{p'p}|^2 \langle\chi_m^\tau|(U_1)_{p'}\sigma_x(U_1^\dagger)_{p'}|\chi_m^\tau\rangle \\ &= \frac{1}{3} \sum_{p'} \langle\chi_m^\tau|[\cos(2\theta_{p'})\sigma_x + \sin(2\theta_{p'})\sigma_y]|\chi_m^\tau\rangle. \end{aligned} \quad (\text{C6})$$

where  $(U_1^\dagger)_1 = e^{i\theta_1\sigma_z}$ ,  $(U_1^\dagger)_2 = -e^{i\theta_2\sigma_z}$ , and  $(U_1^\dagger)_3 = -e^{i\theta_3\sigma_z}$ , with  $\theta_1 = 7\pi/12$ ,  $\theta_2 = 11\pi/12$ , and  $\theta_3 = \pi/4$ . We note that  $\langle\chi_m^\tau|\sigma_y|\chi_m^\tau\rangle = 0$ . Moreover, the trigonometric sums vanish:

$$\sum_{p'} \cos(2\theta_{p'}) = \cos\frac{7\pi}{6} + \cos\frac{11\pi}{6} + \cos\frac{\pi}{2} = 0. \quad (\text{C7})$$

Thus, we have  $s_x(\mathbf{k}) = 0$ . Similarly, we have  $s_y(\mathbf{k}) = 0$ .

## Supplemental Material for “Hidden Zeeman Field in Odd-Parity Magnets: An Ideal Platform for Topological Superconductivity”

This Supplemental Material includes the following six sections: (1) Details of the band structures of model  $H_1$ ; (2) Details of model  $H_2$  (3) Topological superconductors (TSCs) based on models  $H_{1,2}$ ; (4) Engineering TSCs based on 1D Odd-parity magnets (OPMs); (5) Engineer Majorana corner states and Kramers pair; (6) Band structure of the  $p$ -wave magnet  $\text{EuIn}_2\text{As}_2$ .

### A. Details of the band structures of model $H_1$

The model  $H_1$  describes a  $120^\circ$  antiferromagnetic order on a triangular lattice with a  $\sqrt{3} \times \sqrt{3}$  magnetic reconstruction. The magnetic unit cell contains three sublattices (A, B, and C), whose local magnetic moments are, respectively, given by

$$\mathbf{m}_A = \left(-\frac{\sqrt{3}}{2}, -\frac{1}{2}, 0\right), \quad \mathbf{m}_B = \left(\frac{\sqrt{3}}{2}, -\frac{1}{2}, 0\right), \quad \mathbf{m}_C = (0, 1, 0).$$

The real-space Hamiltonian reads

$$H_1(\mathbf{r}) = \sum_{\mathbf{r}, \sigma, \sigma'} J \mathbf{m}(\mathbf{r}) \cdot \mathbf{c}_\sigma^\dagger(\mathbf{r}) \boldsymbol{\sigma}_{\sigma\sigma'} c_{\sigma'}(\mathbf{r}) + t \sum_{\langle \mathbf{r}\mathbf{r}' \rangle, \sigma} c_\sigma^\dagger(\mathbf{r}) c_\sigma(\mathbf{r}'), \quad (\text{S1})$$

where  $c_{\mathbf{r}\sigma}^\dagger$  ( $c_{\mathbf{r}\sigma}$ ) creates (annihilates) an electron with spin  $\sigma$  at the site  $\mathbf{r}$ ,  $\langle \mathbf{r}\mathbf{r}' \rangle$  runs over the nearest-neighbor pairs with hopping amplitude  $t$ , and the second term describes the exchange coupling of strength  $J$  between the electron spin and the local magnetic moment  $\mathbf{m}(\mathbf{r})$ .  $\boldsymbol{\sigma} = (\sigma_x, \sigma_y, \sigma_z)$  are the Pauli matrices and the spatially modulated magnetization is  $\mathbf{m}(\mathbf{r}) = (\cos(\mathbf{Q} \cdot \mathbf{r} + \phi), \sin(\mathbf{Q} \cdot \mathbf{r} + \phi), 0)$ , where  $\mathbf{Q} = \frac{4\pi}{3a}(1/2, \sqrt{3}/2)$  and  $\phi = 7\pi/6$ .

The band structures of  $H_1$  can be elucidated through a unitary transformation that aligns all local magnetic moments along a common direction. This unitary transformation can be chosen as  $U(\mathbf{r}) = e^{-i(\mathbf{Q} \cdot \mathbf{r} + \phi)\sigma_z/2}$ , which satisfies  $U(\mathbf{r})[\mathbf{m}(\mathbf{r}) \cdot \boldsymbol{\sigma}]U^\dagger(\mathbf{r}) = \tilde{\sigma}_x$ . Under this transformation, the Hamiltonian becomes

$$\begin{aligned} \tilde{H}_1(\mathbf{r}) &= U(\mathbf{r})H_1U^\dagger(\mathbf{r}) \\ &= \sum_{\langle \mathbf{r}\mathbf{r}' \rangle, \sigma\sigma'} \tilde{t}_{\sigma\sigma'} \tilde{c}_{\mathbf{r}\sigma}^\dagger \tilde{c}_{\mathbf{r}'\sigma'} + J \sum_{\mathbf{r}, \sigma\sigma'} \tilde{c}_{\mathbf{r}\sigma}^\dagger (\tilde{\sigma}_x)_{\sigma\sigma'} \tilde{c}_{\mathbf{r}\sigma'}, \\ &= t \sum_{\mathbf{r}, \sigma} \left[ e^{-i\mathbf{Q} \cdot \mathbf{a}_1 \tilde{\sigma}_z/2} \tilde{c}_\sigma^\dagger(\mathbf{r}) \tilde{c}_\sigma(\mathbf{r} + \mathbf{a}_1) + e^{-i\mathbf{Q} \cdot \mathbf{a}_2 \tilde{\sigma}_z/2} \tilde{c}_\sigma^\dagger(\mathbf{r}) \tilde{c}_\sigma(\mathbf{r} + \mathbf{a}_2) \right. \\ &\quad \left. + e^{-i\mathbf{Q} \cdot \mathbf{a}_3 \tilde{\sigma}_z/2} \tilde{c}_\sigma^\dagger(\mathbf{r}) \tilde{c}_\sigma(\mathbf{r} + \mathbf{a}_3) + \text{h.c.} \right] + J \sum_{\mathbf{r}, \sigma\sigma'} \tilde{c}_{\mathbf{r}\sigma}^\dagger (\tilde{\sigma}_x)_{\sigma\sigma'} \tilde{c}_{\mathbf{r}\sigma'}, \end{aligned} \quad (\text{S2})$$

where  $\mathbf{a}_1 = (1, 0)a$ ,  $\mathbf{a}_2 = (-1/2, \sqrt{3}/2)a$ ,  $\mathbf{a}_3 = -(\mathbf{a}_2 + \mathbf{a}_1) = (-1/2, -\sqrt{3}/2)a$ ,  $\tilde{\boldsymbol{\sigma}} = U\boldsymbol{\sigma}U^\dagger$ , and  $\tilde{c}_{\mathbf{r}\sigma} = \sum_{\sigma'} U_{\sigma\sigma'}(\mathbf{r}) c_{\mathbf{r}\sigma'}$ . Because  $\mathbf{Q} \cdot \mathbf{a}_1 = \mathbf{Q} \cdot \mathbf{a}_2 = \mathbf{Q} \cdot \mathbf{a}_3 = 2\pi/3 \pmod{2\pi}$ , each hopping term carries the same phase  $e^{-i\pi\tilde{\sigma}_z/3}$ , which accounts the non-relativistic spin splitting (NSS) of  $H_1$ . Although this real-space picture intuitively shows the emergence of a Zeeman field and NSS, it does not fully account for the effects of  $U(\mathbf{r})$  on the boundary conditions. A more precise treatment is obtained by working directly with the Bloch Hamiltonian.

In the sublattice-spin space, the Bloch Hamiltonian  $H_1(\mathbf{k})$  can be written as

$$H_1(\mathbf{k}) = \begin{pmatrix} h_A/2 & T_{AB}(\mathbf{k})\sigma_0 & T_{AC}(\mathbf{k})\sigma_0 \\ T_{BA}(\mathbf{k})\sigma_0 & h_B/2 & T_{BC}(\mathbf{k})\sigma_0 \\ T_{CA}(\mathbf{k})\sigma_0 & T_{CB}(\mathbf{k})\sigma_0 & J\sigma_y \end{pmatrix}, \quad (\text{S3})$$

where  $h_A = -J(\sqrt{3}\sigma_x + \sigma_y)$ ,  $h_B = J(\sqrt{3}\sigma_x - \sigma_y)$ ,  $T_{AB}(\mathbf{k}) = T_{BC}(\mathbf{k}) = T_{AC}^*(\mathbf{k}) = f(\mathbf{k}) = t \sum_{i=1}^3 e^{i\mathbf{k} \cdot \mathbf{a}_i}$ . The unitary transformation  $U(\mathbf{r})$  in the momentum space corresponds to a block-diagonal matrix

$$U_1 = \text{diag}(U_A, U_B, U_C), \quad U_A = e^{i\frac{7\pi}{12}\sigma_z}, \quad U_B = e^{i\frac{11\pi}{12}\sigma_z}, \quad U_C = e^{i\frac{\pi}{4}\sigma_z}. \quad (\text{S4})$$

Applying  $U_1$  yields the transformed Hamiltonian:

$$H_1'(\mathbf{k}) = U_1 H(\mathbf{k}) U_1^\dagger = \begin{pmatrix} J\tilde{\sigma}_x & f(\mathbf{k})e^{-i\frac{\pi}{3}\tilde{\sigma}_z} & f^*(\mathbf{k})e^{i\frac{\pi}{3}\tilde{\sigma}_z} \\ f^*(\mathbf{k})e^{i\frac{\pi}{3}\tilde{\sigma}_z} & J\tilde{\sigma}_x & f(\mathbf{k})e^{i\frac{2\pi}{3}\tilde{\sigma}_z} \\ f(\mathbf{k})e^{-i\frac{\pi}{3}\tilde{\sigma}_z} & f(\mathbf{k})^*e^{-i\frac{2\pi}{3}\tilde{\sigma}_z} & J\tilde{\sigma}_x \end{pmatrix}. \quad (\text{S5})$$

However,  $H'_1$  does not recover the cyclic symmetry in the sublattice indices, which corresponds to the translation symmetry of the original triangular lattice. To restore this symmetry, we apply a diagonal gauge transformation  $U_2 = \text{diag}(I, -I, -I)$ , which leads to

$$H''_1(\mathbf{k}) = U_2 H'_1(\mathbf{k}) U_2^\dagger = \begin{pmatrix} J\tilde{\sigma}_x & -f(\mathbf{k})e^{-i\frac{\pi}{3}\tilde{\sigma}_z} & -f^*(\mathbf{k})e^{i\frac{\pi}{3}\tilde{\sigma}_z} \\ -f^*(\mathbf{k})e^{i\frac{\pi}{3}\tilde{\sigma}_z} & J\tilde{\sigma}_x & f(\mathbf{k})e^{i\frac{2\pi}{3}\tilde{\sigma}_z} \\ f(\mathbf{k})e^{-i\frac{\pi}{3}\tilde{\sigma}_z} & f^*(\mathbf{k})e^{-i\frac{2\pi}{3}\tilde{\sigma}_z} & J\tilde{\sigma}_x \end{pmatrix}. \quad (\text{S6})$$

Defining  $D(\mathbf{k}) = -f(\mathbf{k})e^{-i\frac{\pi}{3}\tilde{\sigma}_z}$  and noting that  $e^{-i\pi\tilde{\sigma}_z} = -1$ , we can write  $H''_1(\mathbf{k})$  in a cyclically symmetric form:

$$H''_1(\mathbf{k}) = \begin{pmatrix} J\tilde{\sigma}_x & D(\mathbf{k}) & D^\dagger(\mathbf{k}) \\ D^\dagger(\mathbf{k}) & J\tilde{\sigma}_x & D(\mathbf{k}) \\ D(\mathbf{k}) & D^\dagger(\mathbf{k}) & J\tilde{\sigma}_x \end{pmatrix}. \quad (\text{S7})$$

Notably,  $H''_1$  corresponds to the real space Hamiltonian  $\tilde{H}_1(\mathbf{r})$  with anti-periodic boundary conditions along the  $\mathbf{a}_1$ ,  $\mathbf{a}_2$ , and  $\mathbf{a}_3$  directions.

To block-diagonalize the Hamiltonian, we perform a discrete Fourier transform in sublattice space  $\tilde{H} = U_3 H''_1 U_3^\dagger$ , where

$$U_3 = \frac{1}{\sqrt{3}} \begin{pmatrix} \sigma_0 & \sigma_0 & \sigma_0 \\ \sigma_0 & \omega\sigma_0 & \omega^2\sigma_0 \\ \sigma_0 & \omega^2\sigma_0 & \omega\sigma_0 \end{pmatrix}, \quad \omega = e^{2\pi i/3}.$$

It is noted that  $H''_1$  exhibits cyclic symmetry with matrix elements  $(H''_1)_{ij} = F_{(j-i) \bmod 3}$  where  $F_0 = J\sigma_x$ ,  $F_1 = D(\mathbf{k})$ ,  $F_2 = D^\dagger(\mathbf{k})$ . The matrix elements of  $U_3$  can be written as  $(U_3)_{mi} = \omega^{mi}/\sqrt{3}$  and those of its adjoint as  $(U_3^\dagger)_{jn} = \omega^{-nj}/\sqrt{3}$  ( $m, n, i, j = 0, 1, 2$ ). Therefore, the  $(m, n)$  element of  $\tilde{H}$  is

$$\tilde{H}_{mn} = \sum_{i,j=0}^2 (U_3)_{mi} (H''_1)_{ij} (U_3^\dagger)_{jn} = \frac{1}{3} \sum_{i,j=0}^2 \omega^{mi} (H''_1)_{ij} \omega^{-nj}. \quad (\text{S8})$$

Using the cyclic form  $(H''_1)_{ij} = F_{(j-i) \bmod 3}$  and introducing the index shift  $k = j - i$  (so that  $j = i + k$ ), the double sum decouples:

$$\tilde{H}_{mn} = \frac{1}{3} \sum_{i=0}^2 \omega^{mi} \left[ \sum_{k=0}^2 h_k \omega^{-n(i+k)} \right] = \frac{1}{3} \left( \sum_{i=0}^2 \omega^{(m-n)i} \right) \left( \sum_{k=0}^2 \omega^{-nk} h_k \right). \quad (\text{S9})$$

The summation over  $i$  yields  $\sum_{i=0}^2 \omega^{(m-n)i} = 3\delta_{mn}$  and we have  $\tilde{H}_{mn} = \delta_{mn} \sum_{k=0}^2 \omega^{-nk} h_k$ . Consequently,  $\tilde{H}$  is diagonal in the sublattice indices, and the transformed Hamiltonian becomes:

$$\tilde{H}(\mathbf{k}) = U_3 H''_1(\mathbf{k}) U_3^\dagger = \text{diag}(h_0(\mathbf{k}), h_1(\mathbf{k}), h_2(\mathbf{k})), \quad (\text{S10})$$

with each block given by

$$h_m(\mathbf{k}) = J\sigma_x + \omega^{-m} D(\mathbf{k}) + \omega^m D^\dagger(\mathbf{k}), \quad m = 0, 1, 2. \quad (\text{S11})$$

The three blocks are not independent. Using the property  $f(\mathbf{k} + \mathbf{Q}) = \omega f(\mathbf{k})$ , one finds  $D(\mathbf{k} + \mathbf{Q}) = \omega D(\mathbf{k})$  and  $D^\dagger(\mathbf{k} + \mathbf{Q}) = \omega^{-1} D^\dagger(\mathbf{k})$ . Consequently,

$$\begin{aligned} h_0(\mathbf{k} + \mathbf{Q}) &= J\tilde{\sigma}_x + \omega D(\mathbf{k}) + \omega^{-1} D^\dagger(\mathbf{k}) \\ &= J\tilde{\sigma}_x + \omega^{-2} D(\mathbf{k}) + \omega^2 D^\dagger(\mathbf{k}) \\ &= h_2(\mathbf{k}), \end{aligned} \quad (\text{S12})$$

and similarly  $h_0(\mathbf{k} - \mathbf{Q}) = h_1(\mathbf{k})$ . Thus, the full spectrum is captured by a single effective two-band Hamiltonian, which we take as

$$\begin{aligned} h_0(\mathbf{k}) &= J\tilde{\sigma}_x - f(\mathbf{k})e^{-i\frac{\pi}{3}\tilde{\sigma}_z} - f^*(\mathbf{k})e^{i\frac{\pi}{3}\tilde{\sigma}_z} \\ &= J\tilde{\sigma}_x - f_0(\mathbf{k})\sigma_0 - f_z(\mathbf{k})\tilde{\sigma}_z, \end{aligned} \quad (\text{S13})$$

where  $f_0(\mathbf{k}) = t \cos k_x a + 2t \cos(k_x a/2) \cos(\sqrt{3}k_y a/2)$  and  $f_z(\mathbf{k}) = \sqrt{3}t (\sin k_x a - 2 \sin(k_x a/2) \cos(\sqrt{3}k_y a/2))$ .

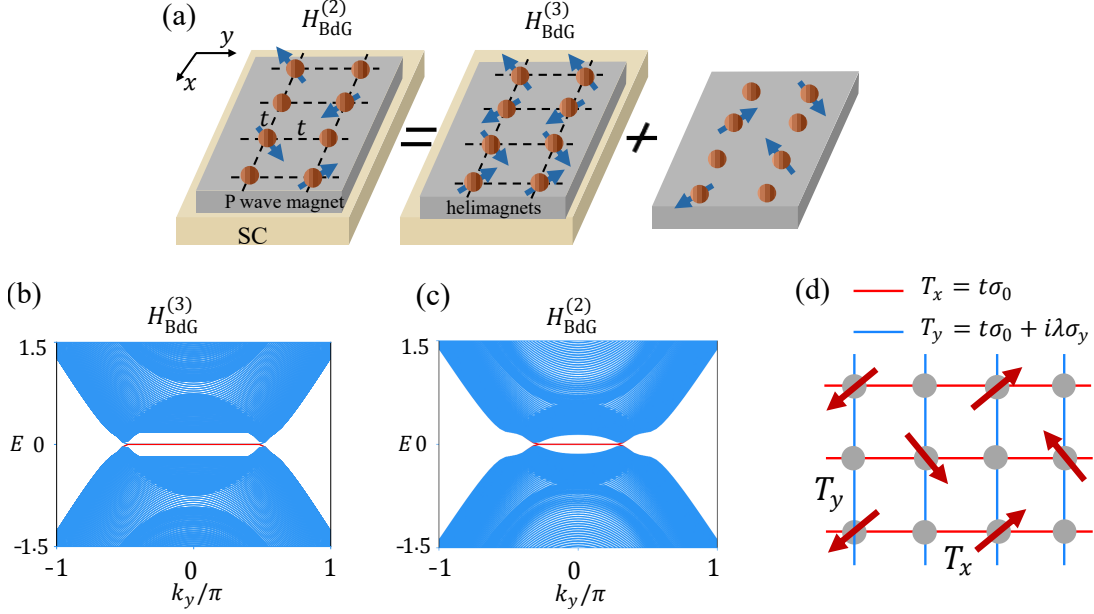


FIG. S1. (a) Schematic illustration of model  $H_{\text{BdG}}^{(2)}$ , mapping it to stacked superconducting 1D helimagnets with additional compensated Zeeman fields. (b) and (c) Energy bands of  $H_{\text{BdG}}^{(3)}$  and  $H_{\text{BdG}}^{(2)}$  in a nanowire geometry along the  $y$  direction. (d) Schematic illustration of considering relativistic spin-orbital coupling term  $i\lambda\sigma_y$  in  $H_2$ . The model parameters are taken as  $t = 1$ ,  $J = 0.5$ ,  $\Delta = 0.2$ ,  $\lambda = 0.1$ , and  $\mu = 3.5$ .

## B. Details of model $H_2$

In this section, we present the details of the model  $H_2$ , which is defined on a square lattice.  $H_2$  contains eight magnetic sublattices labeled A through H. The local magnetic moments are given by

$$\begin{aligned} \mathbf{m}_A &= \left( -\frac{\sqrt{2}}{2}, -\frac{\sqrt{2}}{2}, 0 \right), \mathbf{m}_C = \left( \frac{\sqrt{2}}{2}, \frac{\sqrt{2}}{2}, 0 \right), \mathbf{m}_F = \left( \frac{\sqrt{2}}{2}, -\frac{\sqrt{2}}{2}, 0 \right), \\ \mathbf{m}_H &= \left( -\frac{\sqrt{2}}{2}, \frac{\sqrt{2}}{2}, 0 \right), \mathbf{m}_B = \mathbf{m}_D = \mathbf{m}_E = \mathbf{m}_G = (0, 0, 0). \end{aligned}$$

The arrangement of these magnetic moments is shown in Fig. S1(d).

$H_2$  respects two effective time-reversal operations,  $\tilde{\mathcal{T}}_2 = \tilde{\mathcal{T}}\tau_2$  and  $\tilde{\mathcal{T}}_1 = \tilde{\mathcal{T}}\sigma_z$ , together with a spin group symmetry  $g_3 = \{s_y || M_x | \tau_3\}$ . Here  $\tau_2$  and  $\tau_3$  are half-period translations along  $x$  and  $y$ , respectively, and  $M_x$  denotes a mirror reflection with respect to the  $yz$ -plane. These three symmetries yield the following constraints:

$$\begin{aligned} \tilde{\mathcal{T}}_2: s_z(\mathbf{k}) &= -s_z(-\mathbf{k}), & s_{x,y}(\mathbf{k}) &= s_{x,y}(-\mathbf{k}), \\ \tilde{\mathcal{T}}_1: s_{x,y,z}(\mathbf{k}) &= -s_{x,y,z}(-\mathbf{k}), \\ g_1: s_{x,z}(\mathbf{k}) &= -s_{x,z}(M_x\mathbf{k}), & s_y(\mathbf{k}) &= s_y(M_x\mathbf{k}). \end{aligned} \quad (\text{S14})$$

Consequently, we obtain  $s_z(k_x, k_y) = \pm s_z(\pm k_x, \mp k_y)$  and  $s_{x,y}(\mathbf{k}) = 0$ . By expanding  $s_z(\mathbf{k})$  around the  $\Gamma$  point, the leading term for describing the NSS is  $k_x\sigma_z$ , identifying  $H_2$  as a  $p$ -wave magnet.

## C. TSCs based on models $H_{1,2}$

By introducing  $s$ -wave superconducting pairing into models  $H_1$  and  $H_2$ , we construct the corresponding Bogoliubov–de Gennes (BdG) Hamiltonians, denoted as  $H_{\text{BdG}}^{(1,2)}$ . Hamiltonians  $H_{\text{BdG}}^{(1,2)}$  respect the particle–hole symmetry  $\mathcal{P} = \tau_x K$  and the effective time-reversal symmetry  $\tilde{\mathcal{T}}_2 = \mathcal{T}\sigma_z$ , giving rise to the chiral symmetry  $C = \mathcal{P}\tilde{\mathcal{T}}_2 = \tau_x\sigma_x$ ,

which places the systems in the BDI symmetry class. In two dimensions, this chiral symmetry can stabilize a nodal topology and protect Majorana flat bands as demonstrated in the main text.

Since  $H_1(\mathbf{k})$  can be exactly mapped to the two-band model  $h_0(\mathbf{k})$ , it is convenient to analyze the nodal structure of  $H_{\text{BdG}}^{(2)}$  using  $h_0$ . For  $h_0$  with a  $s$ -wave pairing, the BdG Hamiltonian reads

$$\tilde{h}_{\text{BdG}}^{(1)} = -\tilde{f}_0(\mathbf{k})\tau_z\sigma_0 + J\tau_0\tilde{\sigma}_x - f_z(\mathbf{k})\tau_z\tilde{\sigma}_z + \Delta\tau_y\tilde{\sigma}_y, \quad (\text{S15})$$

where  $\tilde{f}_0 = f_0 - \mu$ . The energy spectrum of  $\tilde{h}_{\text{BdG}}^{(1)}$  is given by

$$E(\mathbf{k}) = \pm \sqrt{J^2 + \Delta^2 + \tilde{f}_0^2 + f_z^2 \pm 2\sqrt{J^2\Delta^2 + J^2\tilde{f}_0^2 + f_z^2\tilde{f}_0^2}}. \quad (\text{S16})$$

Therefore, the energy gap closes when  $f_z(\mathbf{k}) = 0$  and  $J^2 = \Delta^2 + (f_0 - \mu)^2$ . These conditions are satisfied at certain points along the  $\Gamma$ - $M_{1,2,3}$  lines where  $f_z(\mathbf{k})$  vanishes, producing six pairs of nodal points in the Brillouin zone.

As explained in Fig. S1(a), the model  $H_{\text{BdG}}^{(2)}$  can be decomposed into a stack of superconducting helimagnets with additional compensated Zeeman fields. A stack of superconducting helimagnets hosts the nodal topology featuring Majorana flat bands, as shown in Fig. S1(b). While the extra Zeeman fields merely shift the positions of the bulk nodes and flat bands remain, by comparing Fig. S1(c) to Fig. S1(b).

Based on the model  $H_2$ , we further include a relativistic spin-orbital coupling term  $i\lambda\sigma_y$  along the  $y$  direction, as schematically depicted in Fig. S1(d). In the presence of this term, the original Majorana flat bands shown in Fig. S1(c) acquire dispersion and become propagating edge states, while the bulk nodal structure remains intact. This result is displayed in Fig. 3(e) of the main text, where the spin-orbital coupling strength is taken as  $\lambda = 0.1$ .

## D. Engineering TSCs Based on 1D OPMs

OPMs are magnetic systems characterized by a NSS that is odd under spatial inversion, satisfying  $\mathbf{S}(\mathbf{k}) = -\mathbf{S}(-\mathbf{k})$ , where  $\mathbf{S}(\mathbf{k}) = (s_x(\mathbf{k}), s_y(\mathbf{k}), s_z(\mathbf{k}))$ . Based on the dimensionality of  $\mathbf{S}(\mathbf{k})$ , OPMs are classified into three distinct types [24]. Type-I OPMs exhibit collinear spin texture, for example,  $s_z(\mathbf{k}) = -s_z(-\mathbf{k})$  with  $s_x(\mathbf{k}) = s_y(\mathbf{k}) = 0$ . Type-II OPMs possess a coplanar spin texture, where the spins are confined to a plane, for example  $s_z(\mathbf{k}) = 0$  and  $s_{x,y}(\mathbf{k}) = -s_{x,y}(-\mathbf{k})$ . Type-III OPMs are characterized by a non-coplanar spin texture, with all three spin components being nonzero and each obeying  $s_\alpha(\mathbf{k}) = -s_\alpha(-\mathbf{k})$  for  $\alpha = x, y, z$ . Therefore, previously studied 2D models  $H_{1,2}$  belong to type-I OPMs. In this section, we further use three 1D models, which belong to type-I, type-II, and type-III OPMs, respectively, to engineer TSCs.

### D1. Model Hamiltonians and TSCs

Type-I OPMs can be realized in coplanar magnetic orders respecting the spin-group symmetry  $g_1 = \{U_z(\theta)|\tau\}$ , such as the 1D helimagnet described by model  $\mathcal{H}_1$ , as schematically illustrated in Fig. S2(a). Type-II OPMs can be realized in non-coplanar magnetic orders that simultaneously possess the symmetries  $\mathcal{T}\tau$  and  $\{U_z(\pi)|P\}$  (with  $P$  denoting spatial inversion), as implemented in model  $\mathcal{H}_2$ , schematically illustrated in Fig. S2(b). Type-III OPMs are realized in non-coplanar magnetic orders respecting the  $\mathcal{T}\tau$  symmetry, exemplified by model  $\mathcal{H}_3$ , as schematically illustrated in Fig. S2(c).

The model Hamiltonians  $\mathcal{H}_{1,2,3}$  can be expressed in a unified form:

$$\mathcal{H}_n = \sum_{\langle \mathbf{r}\mathbf{r}' \rangle, \sigma} t c_{\mathbf{r}\sigma}^\dagger c_{\mathbf{r}'\sigma} + J \sum_{\mathbf{r}, \sigma\sigma'} \mathbf{m}_n(\mathbf{r}) \cdot c_{\mathbf{r}\sigma}^\dagger \boldsymbol{\sigma}_{\sigma\sigma'} c_{\mathbf{r}\sigma'}, \quad n = 1, 2, 3 \quad (\text{S17})$$

For  $\mathcal{H}_1$ , the local magnetic moment is expressed as  $\mathbf{m}_1(\mathbf{r}) = (\cos(\mathbf{Q}_1 \cdot \mathbf{r}), \sin(\mathbf{Q}_1 \cdot \mathbf{r}), 0)$ , where  $|\mathbf{Q}_1| = 2\pi/\mathcal{L}$ . In Fig. S2(a), we take  $\mathcal{L} = 3$  and  $\mathcal{H}_1$  realizes a  $p$ -wave magnet. When  $\mathcal{L} = 1$  and  $\mathcal{L} = 2$ ,  $\mathcal{H}_1$  describes a conventional ferromagnet and an antiferromagnet, respectively. Models  $\mathcal{H}_2$  and  $\mathcal{H}_3$  have four magnetic sublattices. Their local moments are given by: For  $\mathcal{H}_2$  (sublattices A, B, C, D):

$$\mathbf{m}_2^A = \left( \frac{1}{\sqrt{3}}, \frac{1}{\sqrt{3}}, \frac{1}{\sqrt{3}} \right), \quad \mathbf{m}_2^B = \left( \frac{1}{\sqrt{3}}, \frac{1}{\sqrt{3}}, -\frac{1}{\sqrt{3}} \right), \quad \mathbf{m}_2^C = -\left( \frac{1}{\sqrt{3}}, \frac{1}{\sqrt{3}}, \frac{1}{\sqrt{3}} \right), \quad \mathbf{m}_2^D = \left( -\frac{1}{\sqrt{3}}, -\frac{1}{\sqrt{3}}, \frac{1}{\sqrt{3}} \right).$$

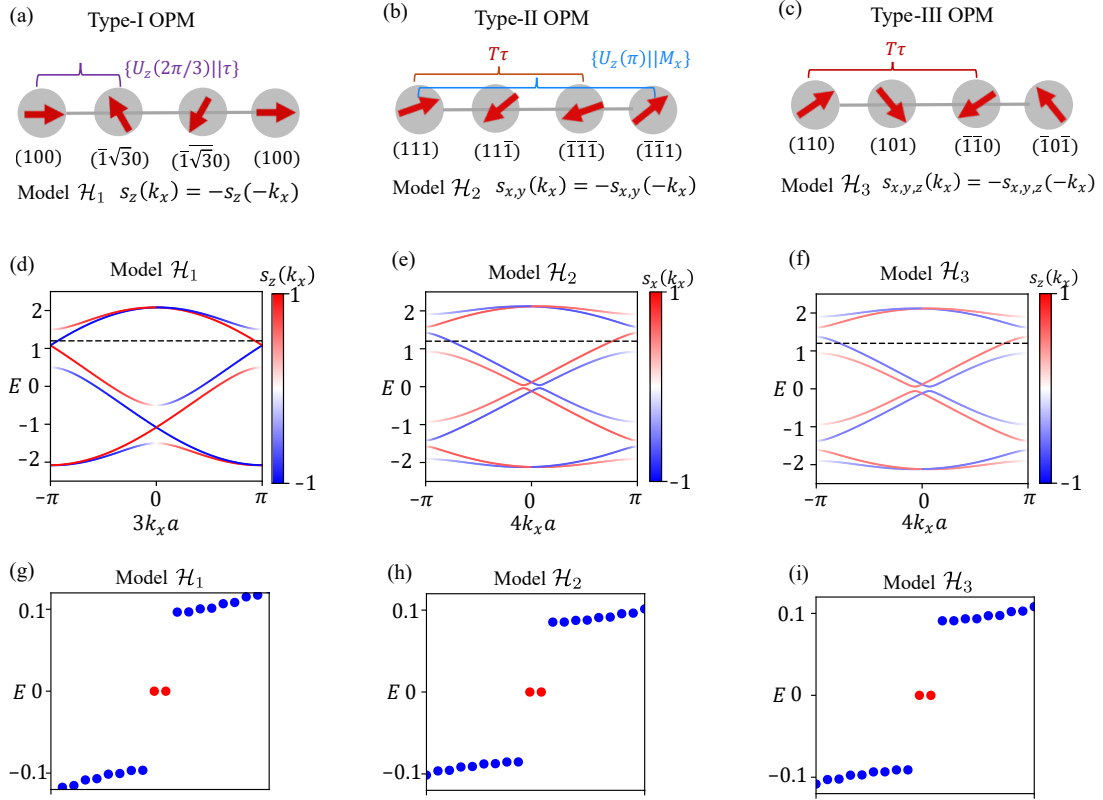


FIG. S2. (a), (b), and (c) Schematic illustration of the theoretical models  $\mathcal{H}_1$ ,  $\mathcal{H}_2$ , and  $\mathcal{H}_3$ , realizing type-I, type-II, and type-III OPMS, respectively. The numbers ( $xyz$ ) beneath the magnetic atoms denote the directional vectors of the local magnetic moments. Solid lines indicate that different magnetic sublattices are related by specific symmetries. (d), (e), and (f) Bulk energy bands for models  $\mathcal{H}_1$ ,  $\mathcal{H}_2$ , and  $\mathcal{H}_3$ , respectively. (g), (h), and (i) Eigenvalues near zero energy for models  $\mathcal{H}_{\text{BdG}}^{(i)}$  under the open boundary conditions. The adopted chemical potential is marked by black dashed lines in (d)–(f), lying within the magnetic gap. The model parameters are taken as  $t = 1$ ,  $J = 0.5$ , and  $\Delta = 0.1$ .

For  $\mathcal{H}_3$  (sublattices A, B, C, D):

$$\mathbf{m}_3^A = \left( \frac{1}{\sqrt{2}}, \frac{1}{\sqrt{2}}, 0 \right), \quad \mathbf{m}_3^B = \left( \frac{1}{\sqrt{2}}, 0, \frac{1}{\sqrt{2}} \right), \quad \mathbf{m}_3^C = \left( -\frac{1}{\sqrt{2}}, -\frac{1}{\sqrt{2}}, 0 \right), \quad \mathbf{m}_3^D = \left( -\frac{1}{\sqrt{2}}, 0, -\frac{1}{\sqrt{2}} \right).$$

Under the corresponding symmetry constraints, their spin textures of models  $\mathcal{H}_{1,2,3}$  satisfy [24]:

$$\begin{aligned} \mathcal{H}_1 : s_z(k_x) &= -s_z(-k_x), \quad s_{x,y}(k_x) = -s_{x,y}(-k_x); \\ \mathcal{H}_2 : s_{x,y}(k_x) &= -s_{x,y}(-k_x), \quad s_z(k_x) = 0; \\ \mathcal{H}_3 : s_{x,y,z}(k_x) &= -s_{x,y,z}(-k_x). \end{aligned} \tag{S18}$$

These relations are fully consistent with the numerical results. The corresponding bulk energy bands of  $\mathcal{H}_{1,2,3}$  are shown in Figs. S2(d)–S2(f).

A key feature in the band structures of  $\mathcal{H}_1$ ,  $\mathcal{H}_2$ , and  $\mathcal{H}_3$  is that for some bands, the Kramers degeneracy at time-reversal invariant momenta is lifted. Specifically, certain energy bands of  $\mathcal{H}_1$  exhibit no Kramers degeneracy at either  $k_x = 0$  or  $k_x = \pi$ , while for  $\mathcal{H}_2$  and  $\mathcal{H}_3$ , energy bands retain degeneracy only at  $k_x = 0$ . This selective lifting of degeneracy in  $\mathcal{H}_{2,3}$  follows from the symmetry  $\tilde{\mathcal{T}}_1 = \mathcal{T}\tau$ , with  $\tilde{\mathcal{T}}_1^2 = -1$  at  $k_x = 0$ . The systematic absence of Kramers pairs at time-reversal momenta in these bands signals the presence of a hidden Zeeman field in OPMS, which opens a magnetic energy gap. With this gap opened, introducing  $s$ -wave superconducting pairing drives the systems into a 1D topological superconducting phase featuring Majorana end modes, as shown in Figs. S2(g)–S2(i).

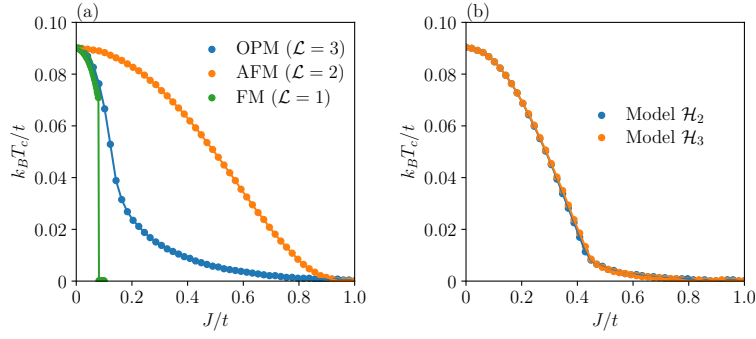


FIG. S3. (a) Self-consistently calculated transition temperature  $T_c$  versus  $J/t$  for model  $\mathcal{H}_{\text{BdG}}^{(1)}$ , showing distinct magnetic phases: OPM with  $\mathcal{L} = 3$ , antiferromagnetic (AFM) with  $\mathcal{L} = 2$ , and ferromagnetic (FM) with  $\mathcal{L} = 1$ . (b) Self-consistently calculated transition temperature for model  $\mathcal{H}_{\text{BdG}}^{(2)}$  and  $\mathcal{H}_{\text{BdG}}^{(3)}$ . The common model parameters are  $t = 1$ ,  $J = 0.5$ ,  $U = 1.5$ , and  $\mu = -1$ .

## D2. Band Structures of the 1D helimagnets

To analytically reveal the band structure of  $\mathcal{H}_1$  for  $\mathcal{L} = 3$ , we perform a local unitary transformation that aligns the magnetic moments along the  $x$ -axis:

$$\tilde{\mathcal{H}}_1 = \mathcal{U}_1 \mathcal{H}_1 \mathcal{U}_1^\dagger, \quad \text{with} \quad \mathcal{U}_1(\mathbf{r}) = e^{-i\mathbf{Q}_1 \cdot \mathbf{r} \sigma_z / 2}. \quad (\text{S19})$$

The transformed Hamiltonian becomes

$$\tilde{\mathcal{H}}_1 = \sum_{\langle \mathbf{r}\mathbf{r}' \rangle, \sigma\sigma'} (\tilde{t}_{\sigma\sigma'} \tilde{c}_{\mathbf{r}\sigma}^\dagger \tilde{c}_{\mathbf{r}'\sigma'} + \text{h.c.}) + J \sum_{\mathbf{r}, \sigma\sigma'} \tilde{c}_{\mathbf{r}\sigma}^\dagger (\tilde{\sigma}_x)_{\sigma\sigma'} \tilde{c}_{\mathbf{r}\sigma'}, \quad (\text{S20})$$

where  $\tilde{c}_{\mathbf{r}\sigma} = \sum_{\sigma'} \mathcal{U}_{\sigma\sigma'}(\mathbf{r}) c_{\mathbf{r}\sigma'}$ , and  $\tilde{t}_{\sigma\sigma'} = t[\mathcal{U}_1(\mathbf{r})\mathcal{U}_1^\dagger(\mathbf{r}')]_{\sigma\sigma'}$ . In the new basis, the hopping  $\tilde{t}_{\sigma\sigma'}$  is  $te^{-i\pi\tilde{\sigma}_z/3}$ , which reveals the original of NSS. The second term reveals the hidden Zeeman field with a strength of  $J$ .

It is important to note that  $\tilde{\mathcal{H}}_1$  restores the translation symmetry of the underlying lattice, which simplifies the analysis and allows us to derive an effective two-band description. In the rotated frame, the periodic boundary conditions are modified to anti-periodic ones [60] and we obtain the Bloch Hamiltonian [55]

$$\tilde{\mathcal{H}}_1(\mathbf{k}) = J\sigma_x - t \cos k_x \sigma_0 - \sqrt{3}t \sin k_x \sigma_z. \quad (\text{S21})$$

The energy bands of  $\mathcal{H}_1(\mathbf{k})$  can be obtained through the band folding of those of  $\tilde{\mathcal{H}}_1(\mathbf{k})$ .

## D3. Compatibility between different types of OPMs and superconductivity

In the main text, we have shown that superconducting pairing is compatible with type-I OPMs with collinear spin textures. In this subsection, we further demonstrate that this is a general characteristic, no matter the spin textures of the OPMs are collinear, coplanar, or non-coplanar.

To describe the superconducting state, we introduce an attractive on-site interaction  $-U$  ( $U > 0$ ) that mediates a  $s$ -wave pairing. The total lattice Hamiltonian is

$$\mathcal{H}_{\text{SC}}^{(i)} = \mathcal{H}_i - U \sum_{\mathbf{r}} c_{\mathbf{r}\uparrow}^\dagger c_{\mathbf{r}\downarrow}^\dagger c_{\mathbf{r}\downarrow} c_{\mathbf{r}\uparrow}, \quad (\text{S22})$$

where  $i = 1, 2, 3$  labels the model. Within the mean-field approximation, the uniform superconducting order parameter is defined as  $\Delta = U \langle c_{\mathbf{r}\downarrow} c_{\mathbf{r}\uparrow} \rangle$ . The corresponding BdG Hamiltonian in momentum space reads

$$\mathcal{H}_{\text{BdG}}^{(i)}(\mathbf{k}) = \begin{pmatrix} H_i(\mathbf{k}) - \mu & i\Delta\sigma_y \\ -i\Delta^*\sigma_y & -H_i^*(-\mathbf{k}) + \mu \end{pmatrix}, \quad (\text{S23})$$

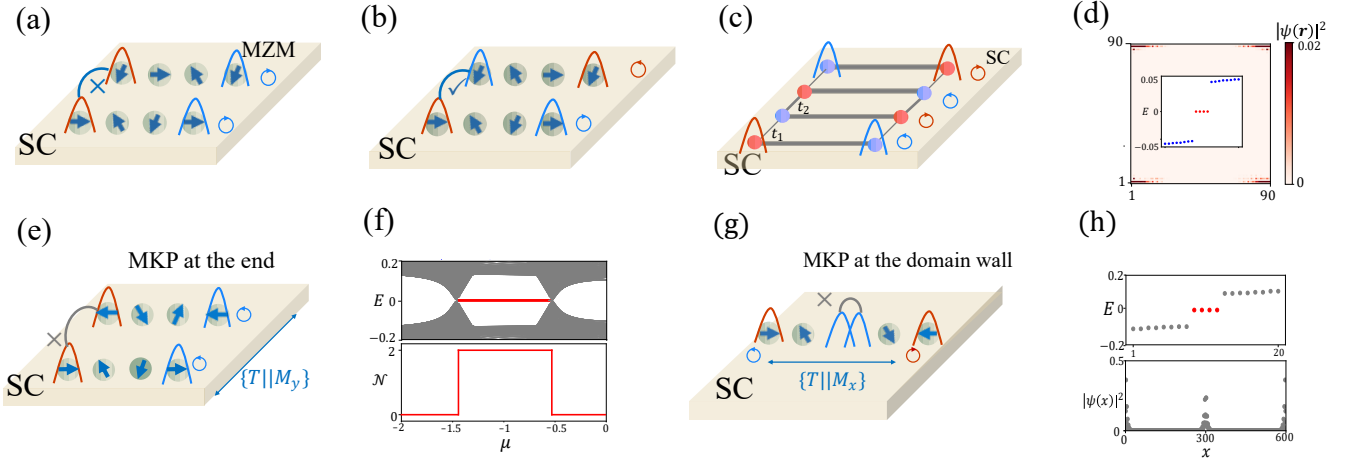


FIG. S4. (a)-(b) Schematic illustration of two helimagnets with (a) identical and (b) opposite spin helicities on superconducting substrates. The two MZMs at one end cannot couple in (a) but can hybridize in (b). (c) Schematic illustration of generating Majorana corner states by a dimerized coupling of 1D TSCs formed by superconducting helimagnets. (d) Spatial distribution of Majorana corner modes in the system shown in (c); the inset displays the low-energy spectrum. (e) Illustration of a Majorana Kramers pairs protected by the spin-group symmetry  $\{T||M_y\}$ . (f) Energy spectrum (upper panel) and spin-resolved Bott index  $\mathcal{N}$  (lower panel) as functions of the chemical potential  $\mu$  for the system in (e). (g) Majorana Kramers pairs localized at a magnetic domain wall, protected by the spin-group symmetry  $\{T||M_x\}$ . (h) Low-energy spectrum (upper panel) and wave functions of the four zero-energy states (lower panel, corresponding to the red dots in the upper panel) for the system in (g). Model parameters:  $t = 1$ ,  $J = 0.5$ ,  $t_1 = 0.1$ ,  $t_2 = 0.3$ ,  $\Delta = 0.2$ , and  $\mu = -1$ . In (f) and (h),  $m_z = 0.1$ .

with  $\mu$  the chemical potential. The mean-field free energy density is

$$\mathcal{F}_s = \frac{|\Delta|^2}{U} - \frac{1}{2\beta V} \sum_{\mathbf{k}, n} \ln(1 + e^{-\beta E_{\mathbf{k}, n}}), \quad (\text{S24})$$

where  $\beta = 1/(k_B T)$ ,  $E_{\mathbf{k}, n}$  are the eigenvalues of  $\mathcal{H}_{\text{BdG}}^{(i)}(\mathbf{k})$ , and  $V$  represents the volume of the system. The critical temperature  $T_c$  is obtained from the linearized gap equation

$$\left. \frac{\partial^2 \mathcal{F}_s(T, \Delta)}{\partial \Delta^2} \right|_{\Delta=0} = 0, \quad (\text{S25})$$

which we solve numerically to obtain  $T_c$ .

Figure. S3(a) shows the normalized critical temperature  $T_c$  as a function of  $J/t$  for model  $\mathcal{H}_{\text{BdG}}^{(1)}$  with different magnetic periods  $\mathcal{L}$ . For the ferromagnetic case ( $\mathcal{L} = 1$ ),  $T_c$  drops sharply because the uniform exchange field fully polarizes the spins and strongly suppresses spin-singlet pairing. In the antiferromagnetic case ( $\mathcal{L} = 2$ ), superconductivity persists up to a larger critical coupling  $J_c/t \simeq 0.9$ . This enhanced stability stems from the spin-degenerate nature of the antiferromagnetic state, which is intrinsically compatible with singlet pairing. For  $\mathcal{L} = 3$ , where  $H_1$  realizes a type-I OPM, superconductivity survives up to  $J_c/t \simeq 0.8$ . Although the net magnetization of this OPM is zero, it exhibits substantial NSS, which reduces the protection compared to a simple antiferromagnet. Nevertheless, the critical  $J_c$  remains significantly higher than that of the ferromagnet, confirming that the odd-parity NSS inherent in the OPM robustly protects the superconducting state from the exchange field.

Notably, the character of the superconducting transition also differs among the three cases. For the ferromagnet ( $\mathcal{L} = 1$ ), the sharp drop in  $T_c$  is consistent with a first-order phase transition. In contrast, for both conventional antiferromagnet ( $\mathcal{L} = 2$ ) and OPM ( $\mathcal{L} = 3$ ),  $T_c$  decreases continuously to zero, indicative of a second-order transition. This continuous behavior reflects the protective role of spin degeneracy (for the antiferromagnet) and the odd-parity NSS (for the OPM), which stabilize the pairing against the in-plane hidden Zeeman field [56, 62–64]. Similar trends are observed for models  $\mathcal{H}_{\text{BdG}}^{(2)}$  and  $\mathcal{H}_{\text{BdG}}^{(3)}$ , as shown in Fig. S3(b), despite the fact that their normal-state spin textures are coplanar and non-coplanar, respectively. In both cases, superconductivity coexists with the magnetic order over a wide range of  $J$ , and  $T_c$  vanishes continuously, characteristic of a second-order transition.

## E. Engineering Majorana corner states and Majorana Kramers pairs

The model  $\mathcal{H}_1$  is directly relevant to the experimental platform of iron atom chains fabricated on superconducting substrates, where the helimagnetic order is stabilized by the Ruderman–Kittel–Kasuya–Yosida interaction [65]. In this section, we use coupled superconducting helimagnets to realize distinct types of TSCs, which could be realized in iron atom chains on superconductors.

### E1. Majorana end modes and corner modes

We consider two coupled helimagnetic chains, each described by the Hamiltonian  $\mathcal{H}_{\text{BdG}}^{(1)}$  introduced before. We assume that the spin helicity  $\chi = \text{sgn}[\mathbf{m}(\mathbf{r}) \times \mathbf{m}(\mathbf{r} + \mathbf{a}_1)]$  of each chain can be tuned [66]. This helicity parameter plays a crucial role in determining the topological properties of the coupled system. The helicity  $\chi$  is reversed under a  $\pi$  spin rotation about the  $y$ -axis, represented by the unitary operator  $U_y(\pi) = \sigma_y$ . Because this rotation anti-commutes with the chiral symmetry operator  $C = \tau_x \sigma_x$ , it also reverses the chirality of Majorana zero modes (MZMs) present in the system, namely the eigenvalue of MZMs under  $C$ . Consequently, the chirality of the MZMs becomes directly linked to the spin helicity  $\chi$  of the underlying chain.

Treating the inter-chain hopping as a weak perturbation, we obtain a simple relation between the helicity configuration and the number of robust MZMs at one end of the coupled system:

$$N = N_+ - N_- = \chi_+ - \chi_-, \quad (\text{S26})$$

where  $N$  counts the net number of robust MZMs at one end,  $N_+$  ( $N_-$ ) denotes the number of MZMs with eigenvalue  $+1$  ( $-1$ ) under  $C$ , and  $\chi_+$  ( $\chi_-$ ) counts the number of chains with helicity  $\chi = +1$  ( $\chi = -1$ ). This relation implies that two chains with the same helicity contribute two MZMs of the same chirality, which cannot hybridize and thus remain degenerate, as schematically illustrated in Fig. S4(a). In contrast, chains with opposite helicities give MZMs of opposite chirality, which can be coupled, as schematically illustrated in Fig. S4(b).

The topological character of such coupled-chain systems can also be directly computed using a real-space Bott index (equivalent to a winding number for 1D systems with chiral symmetry) [67]:

$$N = \frac{1}{4\pi i} \text{Tr} \left[ C \log(MQM^\dagger Q) \right], \quad (\text{S27})$$

where  $M = e^{2\pi i x/L_x}$  (with  $L_x$  the length of the system along  $x$ ),  $Q = 1 - 2 \sum_n |\psi_n\rangle\langle\psi_n|$  is the projector onto the occupied states, and  $|\psi_n\rangle$  are the occupied eigenstates of the BdG Hamiltonian. This index provides a robust tool for exploring the topological phase diagram even in the presence of disorder or magnetic fluctuations.

Beyond 1D Majorana end modes, the chiral symmetry  $C$  can protect 2D higher-order TSCs that host Majorana corner modes. This phase can be realized by a dimerized coupling of superconducting helimagnets with alternating spin helicities, as illustrated in Fig. S4(c). Because adjacent chains have opposite helicities, the Majorana end modes of the underlying 1D TSCs (oriented along  $x$ ) couple through the inter-chain hopping along  $y$ . At the two edges  $x = -L_x/2$  and  $x = L_x/2$ , these modes form an effective 1D Kitaev chain along the  $y$  direction. When the intracell hopping  $t_1$  is smaller than the intercell hopping  $t_2$  ( $|t_1| < |t_2|$ ), this edge Kitaev chain itself becomes topological and harbors MZMs at its ends. Under full open boundary conditions, this results in four Majorana corner modes, as shown in Fig. S4(d). This higher-order TSC is characterized by a Bott index  $\tilde{N}$ , obtained from Eq. (S27) by replacing the unitary matrix  $M$  with  $\tilde{M} = e^{2\pi i xy/(L_x L_y)}$ , where  $L_y$  is the length of the system along  $y$  [67].

### E2. Spin-group-symmetry-protected Majorana Kramers pairs

Although time-reversal symmetry  $\mathcal{T}$  is explicitly broken in magnetic systems, certain composite anti-unitary symmetries  $\tilde{\mathcal{T}}$  that satisfy  $\tilde{\mathcal{T}}^2 = -1$  can be preserved. Such symmetries place a superconducting system in the DIII symmetry class and can protect Majorana Kramers pairs, allowing a  $Z_2$  classification.

Specifically, we consider two coupled helimagnets with opposite magnetic moments on a superconducting substrate, as schematically illustrated in Fig. S4(e). This configuration respects the spin group symmetry  $\tilde{\mathcal{T}} = \{\mathcal{T} | M_y\}$ , where  $M_y$  flips  $y$  and  $\tilde{\mathcal{T}}^2 = -1$ . Each helimagnet contributes one Majorana end mode, and the two end modes are related by  $\tilde{\mathcal{T}}$ , forming a Kramers pair. This pair remains robust against any perturbation that preserves  $\tilde{\mathcal{T}}$ , including a finite out-of-plane magnetization component  $m_z$ , as long as the composite symmetry is maintained. To diagnose the

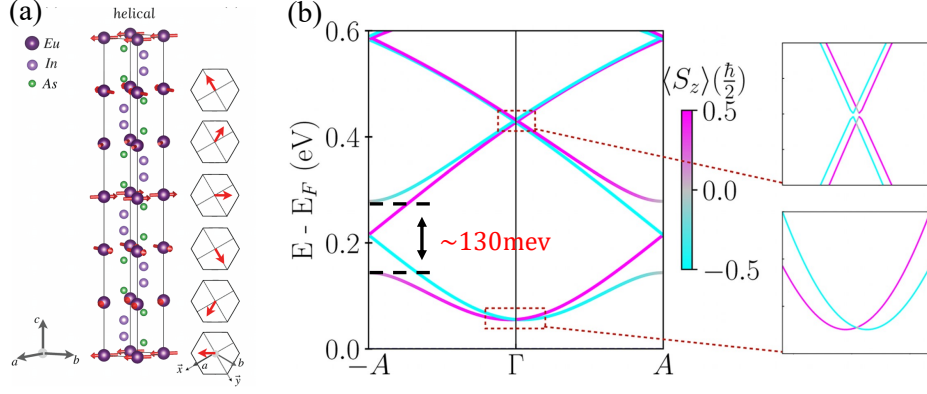


FIG. S5. (a) Coplanar magnetic textures of  $\text{EuIn}_2\text{As}_2$ . (b) Spin-polarized energy bands without SOC of the helical phase along the  $-A$ - $A$  path, where  $A = (0, 0, \pi)$  in reciprocal lattice units. The color encodes the out-of-plane spin expectation value. The small plots on the right are zoomed-in views near the  $\Gamma$  point. The figures are adopted in Ref. 61

presence of such protected Kramers pairs, we employ a spin-resolved Bott index  $\mathcal{N}$ , defined by Eq. (S27) with the unitary matrix  $M$  replaced by  $\mathcal{M} = e^{2i\pi x\sigma_z/L_x}$  [67]. Although spin is not conserved, this index accurately captures the  $\mathbb{Z}_2$  topology associated with the Kramers pair, as demonstrated numerically in Fig. S4(f).

Majorana Kramers pairs can also be realized in a magnetic domain-wall geometry. Figure. S4(g) shows a 1D chain with a domain wall at  $x = 0$  where the helicity changes sign. This setup respects the spin group symmetry  $\tilde{\mathcal{T}} = \{\mathcal{T}||M_x\}$  with  $M_x$  being the spatial mirror operation along the  $x$  direction. Superconducting pairing drives both left and right segments into 1D topological phases, giving rise to two MZMs localized at the domain wall [Fig. S4(h)]. These two MZMs are related by  $\tilde{\mathcal{T}}$  symmetry and thus form a protected Kramers pair.

### F. Band structure of the $p$ -wave magnet $\text{EuIn}_2\text{As}_2$

Material  $\text{EuIn}_2\text{As}_2$  is a candidate  $p$ -wave magnet [24], which crystallizes in a hexagonal structure and hosts a helical spin configuration, as shown in Fig. S5(a). This compound belongs to the spin space group  $P_{6_{001}}^1 6_3/2_{100} m^1 m^1 c(1, 1, 3_{001}^1)^m 1$  [24] and respects the effective time-reversal symmetry  $\tilde{\mathcal{T}}_1 = \mathcal{T}\sigma_z$  and a spin-group symmetry  $g_2 = \{3_{001}^1||1|\tau\}$ , which constrain the spin expectation values to satisfy  $s_{x,y}(\mathbf{k}) = s_{x,y}(-\mathbf{k})$  and  $s_z(\mathbf{k}) = -s_z(-\mathbf{k})$ . The out-of-plane component  $s_z(\mathbf{k})$  transforms as the  $A_{2u}$  representation of the point group  $6/mmm$ , with the basis function  $z$ , see details in the supplemental materials of Ref. 24. Consequently, the leading term of the NSS in the low-energy expansion can be effectively described by  $k_z\sigma_z$ , in agreement with first-principles calculations shown in Fig. S5(b).

Moreover, the system respects the spin-group symmetry  $g_3 = \{-1||6_{001}|\tau_{0,0,0.5}\}$ , [6]. Along the  $\Gamma$ - $A$  line with  $A = (0, 0, \pi)$  in reciprocal lattice units,  $g_2$  acts as an effective time-reversal operation with  $g_2^2 = -e^{ik_z}$ . This guarantees Kramers degeneracy at  $k_z = 0$ , while the degeneracy at  $k_z = \pi$  can be lifted by the broken time-reversal symmetry, as clearly seen in the first principle calculated bands shown in Fig. S5(b). The opened magnetic energy gap is approximately 130 meV. This large intrinsic gap, far exceeding the scale achievable by practical laboratory magnetic fields, exemplifies a key advantage of OPMS as a robust, field-free platform for engineering TSCs.